NEAR GRAZING, SPECULAR SCATTERING OF UNDERWATER SOUND FROM SEA TO SWELL

by

Ned Henderson Mayo

United States
Naval Postgraduate School

THESIS

NEAR-GRAZING, SPECULAR SCATTERING

OF UNDERWATER SOUND FROM SEA AND SWELL

by

Ned Henderson Mayo

December 1969

Near-Grazing, Specular Scattering of Underwater Sound from Sea and Swell

by

Ned Henderson Mayo
Lieutenant Commander, United States Navy
B.S., Georgia Institute of Technology, 1958

Submitted in partial fulfillment of the
requirements for the degree of

MASTER OF SCIENCE IN PHYSICS

from the

NAVAL POSTGRADUATE SCHOOL
December 1969

ABSTRACT

The surface of a large, anechoic tank was excited to produce several different anisotropic sea and swell surfaces characterized by "typical" but distinctive frequency spectra and wave height probability densities. Surface roughness for specular scatter, g ($=4k^2\sigma^2\sin^2\theta$), was varied from zero to four by selection of underwater sound propagation constant, k, RMS wave height, σ, and grazing angle, θ. Concurrent measurement was made of 20 second averages of squared surface wave height, and coherent specularly-scattered sound intensity. For $g \leq 1.$, coherent specular scatter from all surfaces, including pure swell (with a strongly non-Gaussian wave height probability density) was found to vary as e^{-g}, as previously predicted for Gaussian surfaces only. For certain combinations of θ, σ, and sound wavelength, λ, coherent components significantly larger than predicted were noted in both cross-wind and down-wind scattering for $g > 1.$; this is believed to be a previously-hypothesized interference phenomenon. Cross-sea scattering consistently produced a slightly stronger coherent component of intensity than scattering in the direction of the sea.

TABLE OF CONTENTS

LIST OF ILLUSTRATIONS

ACKNOWLEDGEMENT

The author is indebted to his Thesis Advisor, Dr. H. Medwin of the Naval Postgraduate School, for his patient guidance, for his appreciation of the pitfalls of experimental acoustics, and for the insight gained during many hours of fruitful discussion.

Thanks are also due to Mrs. R. S. Lande for her computer programming assistance, and to William Smith for his invaluable aid in obtaining, installing, and maintaining the equipment used.

I. INTRODUCTION

The last ten years have witnessed the development and deployment of low-frequency, high-power, surface ship sonars. Intelligent use of these long-range sensors, and the ability to predict their performance under a given set of conditions, require quantitative understanding of the sound propagation involved. Both surface and seabed reflections of the beam can greatly affect sonar performance; quantitative analysis of "bottom-bounce" phenomena generally has not proved fruitful because of the dearth of knowledge concerning the geography, topography, composition, and acoustic properties of the ocean bottom. Analysis of surface scattering, however, is more tractable because of the comparative ease with which the properties of the reflecting boundary may be studied. In addition, surface scattering experiments are easily scaled to laboratory dimensions.

When a beam of underwater sound is incident upon the water's surface it is scattered, the nature of this scattering being dependent upon the characteristics of the interface. If the surface is smooth, the scattering will be purely specular. Conversely, if the surface is rough, sound will be scattered in all directions, with signal strength being a function of the angle of observation. Rough-surface reflection produces a scattered sound field which contains both coherent and incoherent pressure components relative to the incident pressure. The behavior of the coherent, scattered component is of prime importance because of the increasingly more common use of correlation detectors in sonar systems.

Scheible and Fowler (1968) studied specular scatter of underwater sound from a wind driven model sea at the Naval Postgraduate School;

their investigation included both the amplitude distribution and the frequency spectrum of the scattered sound.

The work reported herein is essentially an extension and refinement of the work done by Scheible. An analogue correlator (which Scheible did not have) was used to isolate the coherent component of the scattered sound pressure. As will be explained in a later section, this isolation permitted the use of much "rougher" water surfaces for scattering. The types of scattering surfaces used were increased to include pure swell, sea-swell combination, and wind driven seas of three different heights. In addition, scattering both parallel and perpendicular to the sea direction was studied.

For all of these "seas" the objective has been to use the model experiment to study cases that are beyond the capability of theorists, and beyond the practicality of ocean-acoustic experiments.

II. THEORETICAL BEHAVIOR OF THE SCATTERED SOUND

A. THE SPECULARLY SCATTERED INTENSITY

The following treatment briefly summarizes the statistical approach of Medwin [Ref. 1], which in turn follows the development of Beckmann [Ref. 2]. The measure of the roughness of the water surface from which the sound is scattered is defined by the roughness parameter g.

$$g = \left[2\pi \frac{\sigma}{\lambda} (\cos \phi_1 + \cos \phi_2)\right]^2$$

where:
- σ = Root-mean-squared (RMS) Wave Height
- λ = Wavelength of sound in water
- ϕ_1 = Angle of incidence of sound upon the surface (measured with normal to surface)
- ϕ_2 = Angle of reflection of the sound

For specular scatter, $\phi_1 = \phi_2 \equiv \phi$ and g becomes

$$g = k^2\sigma^2(2 \cos \phi)^2 = 4k^2\sigma^2\cos^2\phi \qquad \text{where: } k = \frac{2\pi}{\lambda} = \frac{2\pi f}{c}$$

The general scattering problem is then attacked by applying the Helmholtz Integral to a volume within the water, part of the surface of which is the ensonified surface area. If the Kirchhoff assumption (the use of the plane wave reflection coefficient at each point on the surface) is satisfied, an expression for the time-averaged, reflected intensity relative to mirror surface intensity results, which, for the specular direction reduces to:

$$\left\langle \frac{I_{rough}}{I_{mirror}} \right\rangle = e^{-g} + f(A,L,\phi,\sigma,\lambda)$$

where L = Correlation distance on the rough surface

A = Ensonified surface area

I = p*p where p = acoustic pressure

The above expression was derived for a surface correlation function of Gaussian form, and for a Gaussian distribution of surface wave heights.

The first term, describing the coherent specular component, is identical to that obtained by several authors. The second term represents scattered sound which is incoherent with the transmitted signal; since it was not possible to experimentally isolate the very small incoherent component, the exact form of the term is not given here. However, the following theoretical conclusions are considered worthy of note:

1. The magnitude of the incoherent term is a function of ensonified area and correlation distance, while the coherent term, e^{-g}, is independent of these parameters.
2. In the mirror surface limit ($g \to 0$) the incoherent term vanishes, and the coherent component approaches unity.

Scheible [Ref. 3] used this limiting behavior to suppress the incoherent term; he limited g to $0 < g < 0.3$, stated that the first term was much greater than the second, and dropped the incoherent term.

Attacking the problem through the surface wave spectrum, Parkins [Ref. 4] also predicts a coherent term of the form e^{-g}. His incoherent term arises from selective interactions between appropriate surface wave and sound wavelengths. In the purely specular direction, zero incoherent component is predicted, since his treatment considers only the central ray and neglects scattering contributions from off-axis parts of the ensonified area.

B. SURFACE SHADOWING AT NEAR GRAZING INCIDENCE

As the grazing angle (complement of angle of incidence, ϕ) approaches zero, shadowing of certain areas of the scattering surface will result. A shadowing correction, derived from ray acoustics and a statistical representation of the surface, is presented by Wagner [Ref. 5], who states that the correct use of the shadowing function, $S(\theta)$, for the coherent scattered component is:

$$\left\langle \frac{I_{coherent}}{I_{mirror}} \right\rangle = S^2(\theta)\, e^{-g}$$

where: $S(\theta) = (1 - e^{-4B})\, \mathrm{erf}(\frac{v}{4B})$

$$B = \frac{1}{4}\left[(3\pi v)^{-1/2}\, e^{-(9v^2)/8} + (\pi v)^{-1/2}\, e^{-v^2} - \mathrm{erfc}\ v\right]$$

$$v = \frac{\tan\theta}{2(\sigma/L)}$$

σ = RMS wave height

L = Surface correlation distance

θ = Grazing angle

Diffraction effects are neglected by the ray treatment; it is therefore expected that the accuracy of Wagner's correction will increase with increasing $\frac{\sigma}{\lambda}$.

III. EXPERIMENTAL PROCEDURE

A. THE ANECHOIC TANK

The scattering experiments were carried out in the north anechoic tank, filled with fresh water, and of dimensions 24' long, 6' wide, and 8' deep. A wall and bottom lining of acoustically absorbant rubber material renders the tank essentially anechoic at frequencies above 20 kHz. A swell maker and wind-wave generator were located at the east end of the tank as shown in figure 1. Clear plastic covers, suspended 6" above the water, confined the wind generator's output to the surface, producing a wind-driven sea. Five separately controllable, centrifugal fans feeding a common plenum provided the flexibility needed to produce RMS wave heights from 0.1 to 0.5 cm. Swell waves were produced by sinusoidally oscillating a "V" shaped wooden wedge in the vertical plane by means of a motor-driven eccentric, as shown in figure 2.

The sea, swell, or sea-swell combination propagated down the tank, past the sound scattering area, and was largely dissipated by a sloping "beach" consisting of loosely packed aluminum shavings within a plastic screen enclosure. In all cases the ensonified area was centered on the wave staff, which was located at a fetch distance of 3.32 meters measured from the plenum discharge.

The surface area ensonified by the active transducer can be computed geometrically by assuming no ensonification outside the -3dB angles. The resulting surface is an ellipse, whose area, A, and largest linear dimension, d, are computed as shown in figure 3. Attention is invited to the distinction between grazing angle, θ, and its complement, angle of incidence, ϕ. The grazing angle, θ, was determined by measuring transducer separation and transducer depth.

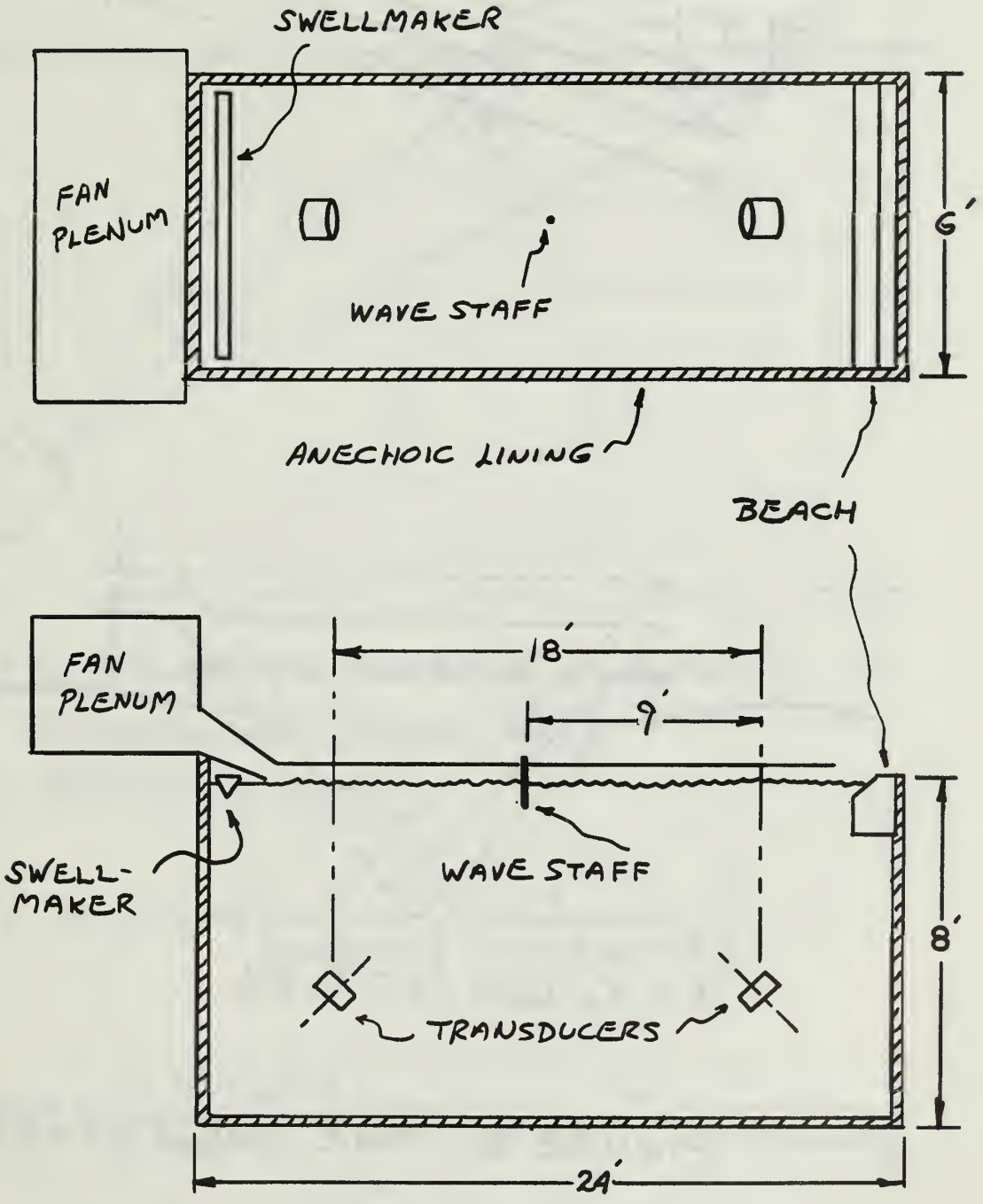

FIGURE 1. THE ANECHOIC TANK

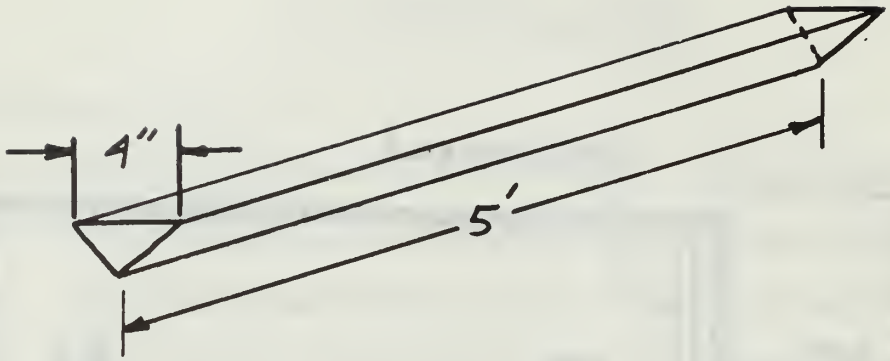

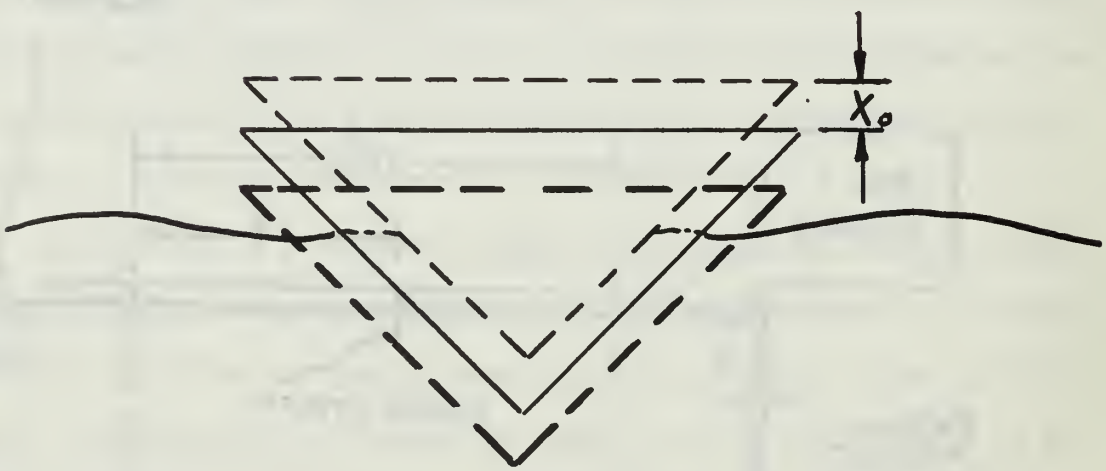

$$X = X_o \cos(2\pi f_o t)$$

FIGURE 2. THE SWELLMAKER

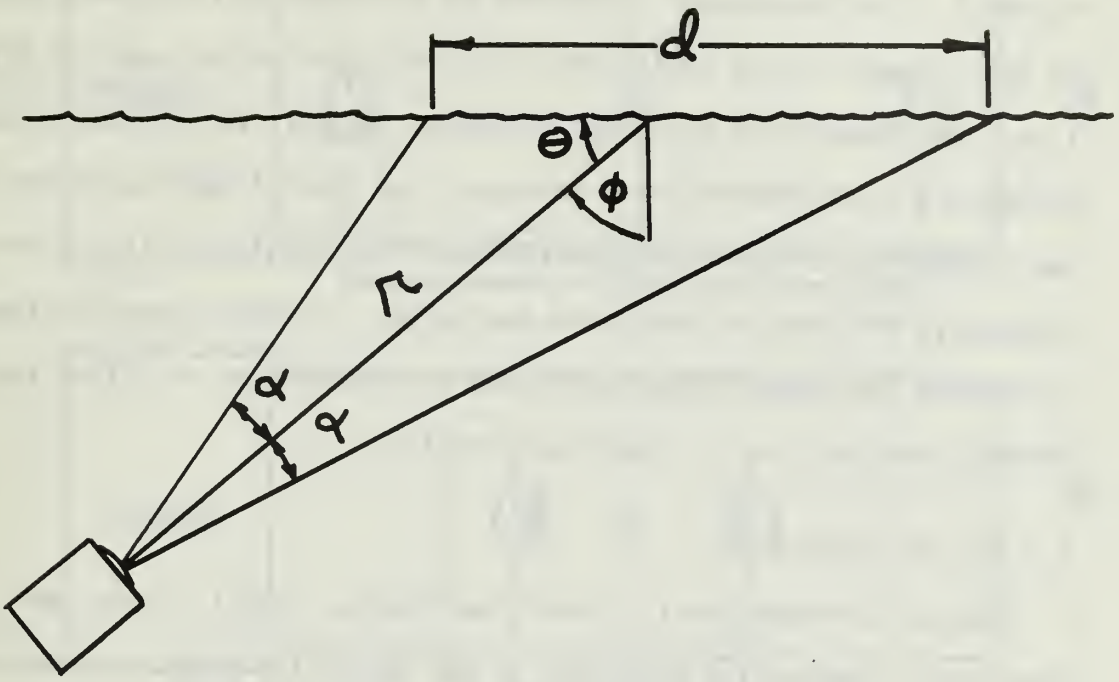

r = DISTANCE TO SURFACE ALONG TRANSDUCER BEAM AXIS

α = BEAM WIDTH

$$d = r \sin\alpha \left[\frac{1}{\cos(\phi+\alpha)} + \frac{1}{\cos(\phi-\alpha)} \right]$$

$$\text{AREA} = \frac{\pi r^2 \sin^2\alpha}{2\cos\alpha} \left[\frac{1}{\cos(\phi-\alpha)} + \frac{1}{\cos(\phi+\alpha)} \right]$$

FIGURE 3. COMPUTATION OF ENSONIFIED AREA

To scatter sound both parallel and perpendicular to the sea direction, three separate transducer arrangements were used as shown in figure 4. The transducers, supported by the mounting racks described in Ref. 1, were always positioned with their axes in the specular direction. For frequencies up to and including 120 kHz, two EDO model 327 piezoelectric transducers were employed; the face of each consisted of two concentric, electrically separated driving sections. At a given frequency, two beam patterns were available: a broader beam obtained by driving the inner section only, and a narrower beam resulting from driving both sections in electrical parallel.

B. THE SEA SURFACE

Various surfaces consisting of "sea" alone, "swell" alone, and "sea-swell" combination were used in the scattering study. To determine the nature of each scattering surface the instantaneous wave height, $z(t)$, at the center of the ensonified area was continuously monitored by an omnidirectional wave staff; the resulting wave record was tape recorded. Upon completion of a particular scattering study, the corresponding wave data were replayed and processed to determine the RMS wave height which existed at the time of the sound scattering.

1. The Wave Staff

The wave staff and its associated electrical circuitry was designed, fabricated, and calibrated locally. The staff, shown in figure 5, is of the resistance type and operates as one leg of a balanced resistance bridge, as shown in figure 6.

Over a limited range of immersion the resistance between the staff and ground rod is inversely proportional to the depth of immersion, and it is within this linear range that the staff is made to operate, as shown in figure 9A.

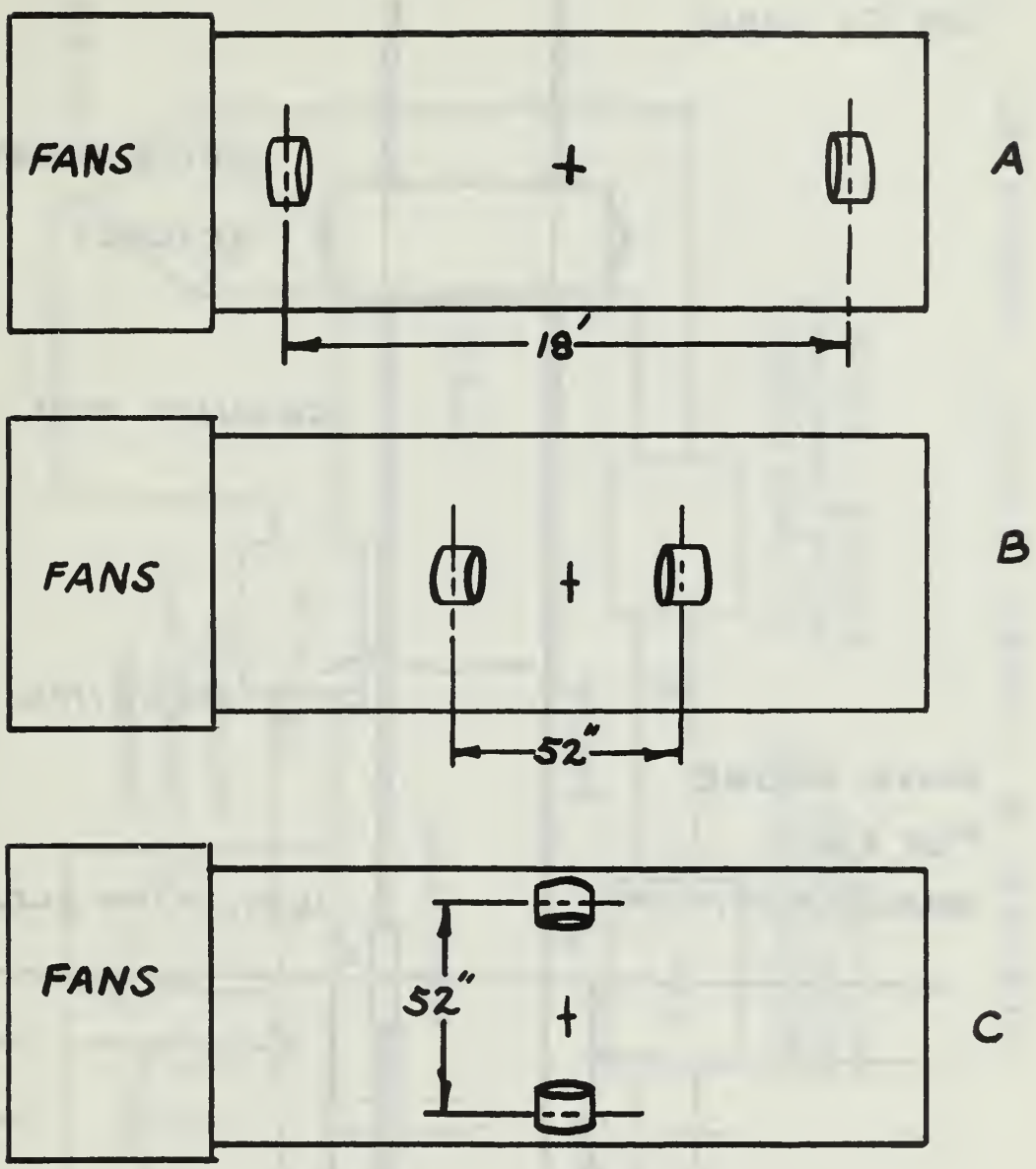

ARRANGEMENT "A" USED TO STUDY SHADOWING. "B" AND "C" USED TO COMPARE PARALLEL AND NORMAL SCATTER.

FIGURE 4. TANK ARRANGEMENTS

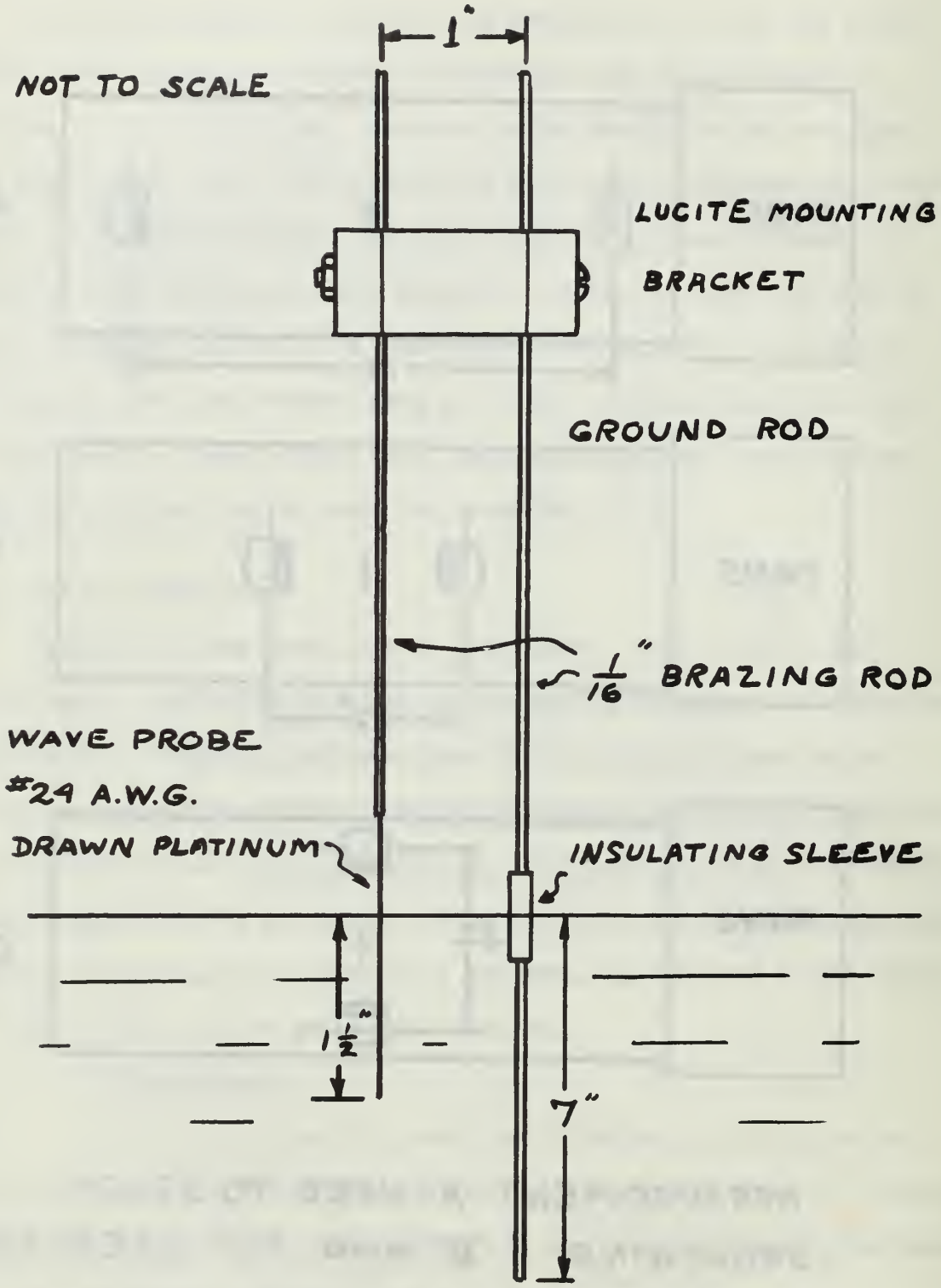

FIGURE 5. WAVE STAFF ASSEMBLY

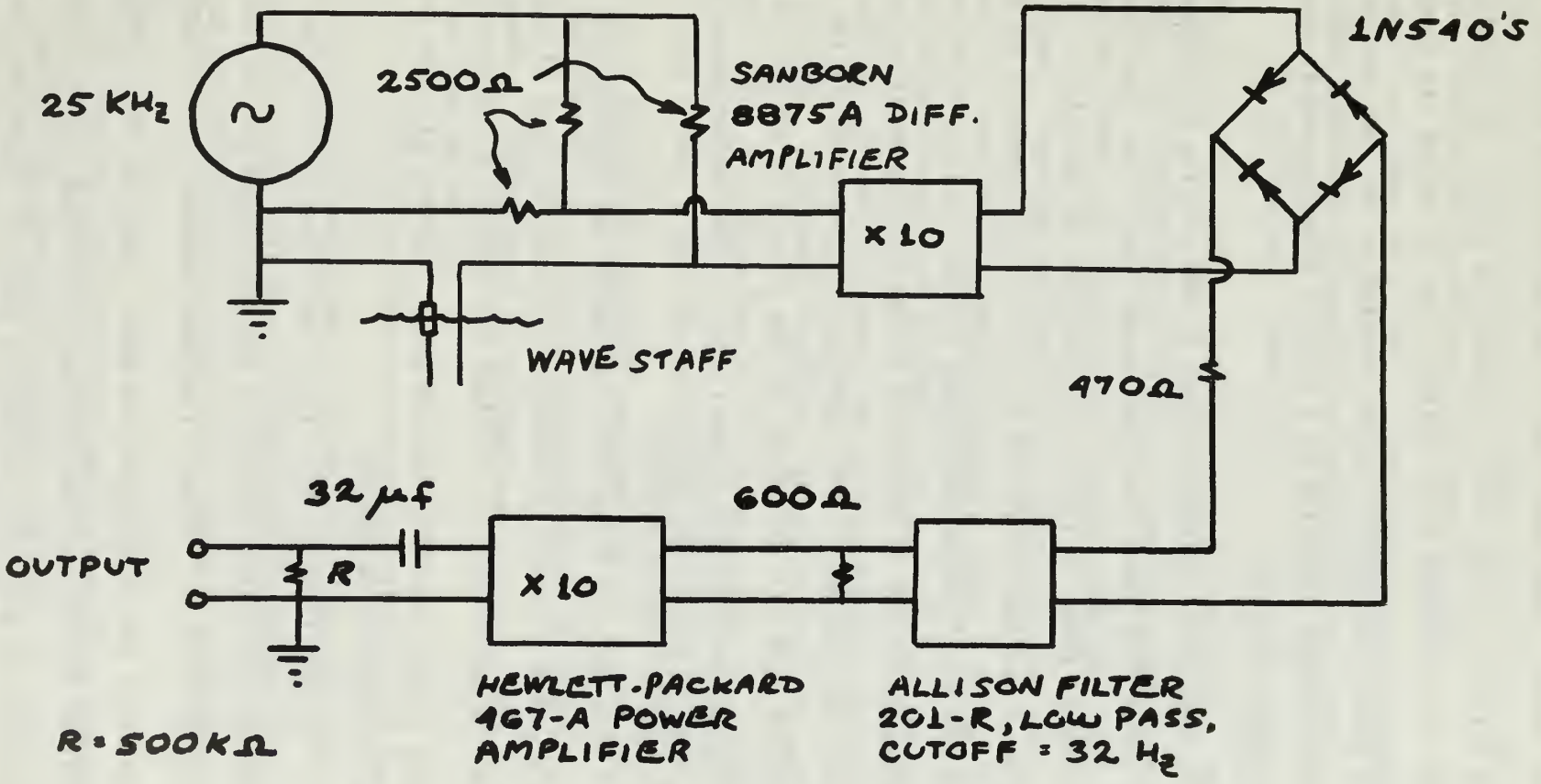

FIGURE 6 WAVE STAFF CIRCUITRY

Preliminary experimentation revealed that the position of the ground rod relative to the staff affected the static calibration of the instrument. To eliminate this variable, and to insure its insensitivity to passing waves, the ground rod was mounted on the same support bracket as the staff and was insulated by a plastic sleeve where it pierced the water's surface (figure 5).

The wave staff assembly formed a time-varying resistance whose mean value was about 2500 ohms; the other three legs of the nearly-balanced resistance bridge, shown in figure 6, were 2500 ohm resistors. This bridge was fed with AC voltage at 25 kHz to prevent the formation of electrolysis bubbles on the staff, which would have caused a change in resistance. The bridge output, a 25 kHz voltage with a time-varying envelope, was amplified, demodulated, and reduced to zero mean by a high-pass RC filter with half-power point of 0.05 Hz. The output of the circuit is called the wave record, $z(t)$, a time-varying voltage proportional to the instantaneous wave height.

a. Wave Staff Calibration

The data of figure 9A (from which was computed the static probe calibration) were obtained by measuring changes in probe circuit output voltage as the water level in the tank was changed by accurately measured increments; it was necessary to take these readings with the DC blocking capacitor of figure 6 by-passed.

In addition to this static deflection calibration, the wave staff (and its associated circuitry) was calibrated for surface wave frequencies up to 30.0 Hz. At each frequency checked, an independent determination of the calibration was made. Each was then normalized (figure 9B) by dividing by the previously obtained static calibration. When the resulting data were plotted as shown in figure 9B, the frequency response curve for the probe and its circuitry results. In the frequency

range $0.5 \leq f \leq 8.0$ Hz, motion of the water relative to the staff was obtained by vertically oscillating the staff assembly in a beaker of "tank water", as shown in figure 7. The frequency and amplitude of this displacement were both adjustable and accurately measurable.

In the frequency range $8.0 \leq f \leq 30.0$ Hz, change in probe immersion was accomplished by generating capillary waves on the surface of a small tank. Referrring to figure 8, the generating mechanism was a lightweight fiber cone, mounted point down, partially beneath the surface as shown. The cone was driven sinusoidally in the vertical plane by an electric vibrator (a permanent magnet, moving coil device) mounted rigidly above the tank. The frequency and amplitude of the cone's motion could be varied by changing the corresponding properties of the driving voltage. To prevent capillary reflection from the walls of the rectangular tank, a sloping "beach" of blotting paper was installed along all four sides. Capillary height was measured both by the wave staff and by a micrometer assembly, mounted rigidly to the frame of the tank, by means of which a thin, pointed rod could be lowered to touch the water's surface. Measurement of maximum wave height by the micrometer assembly was done as follows:

1. With the surface in a mirror condition, the rod was slowly and carefully lowered until its point just touched the surface. Reading the micrometer dial gave a surface height reading accurate to $\pm$.02 mm; to reduce this uncertainty, five consecutive readings were taken and averaged.

2. Capillary waves of the desired frequency were then generated, and the above measurement repeated. The point of first contact in this case was the height of the crests of the waves.

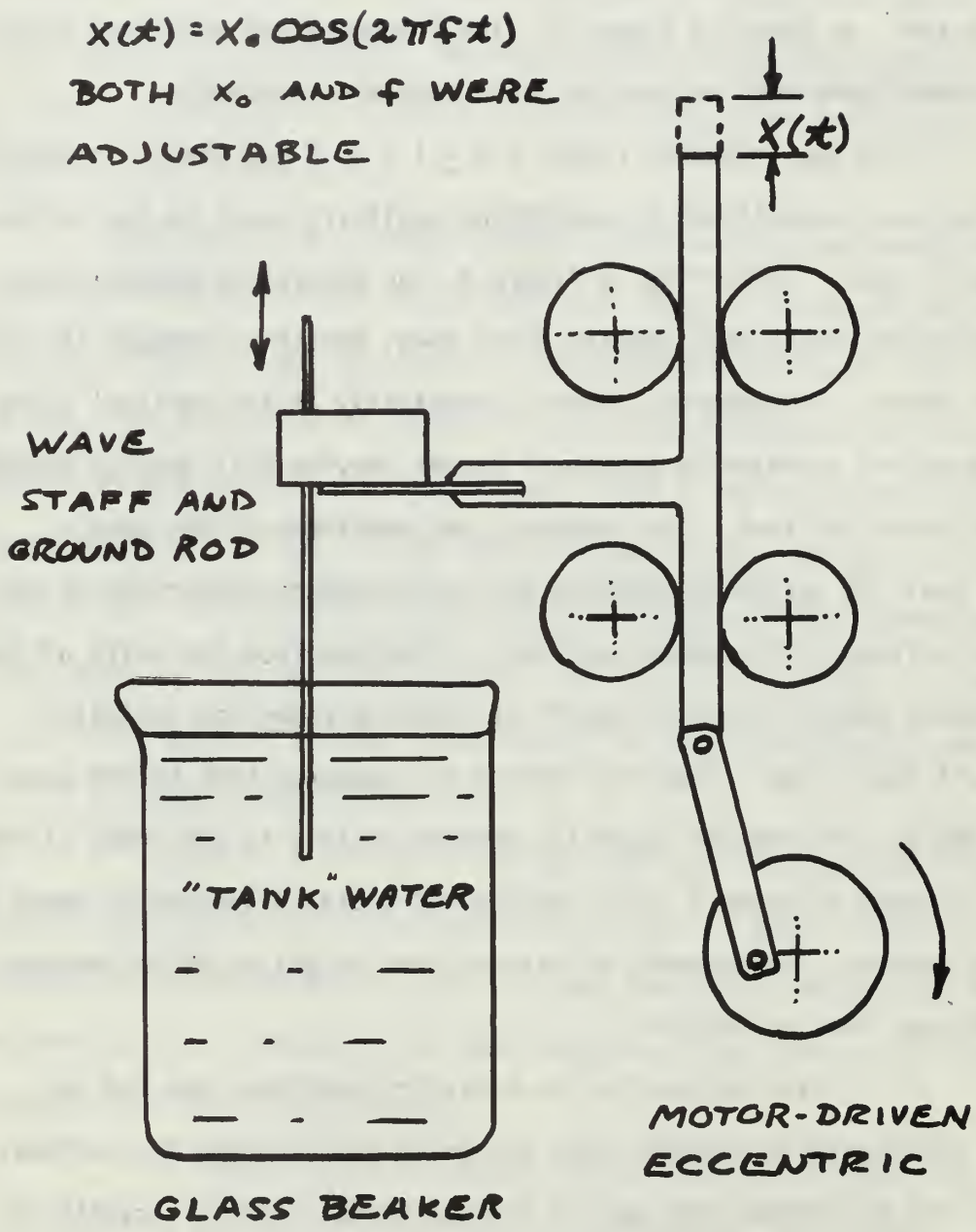

FIGURE 7. WAVE STAFF CALIBRATION FOR $0.5 \leq f \leq 8.0$ Hz

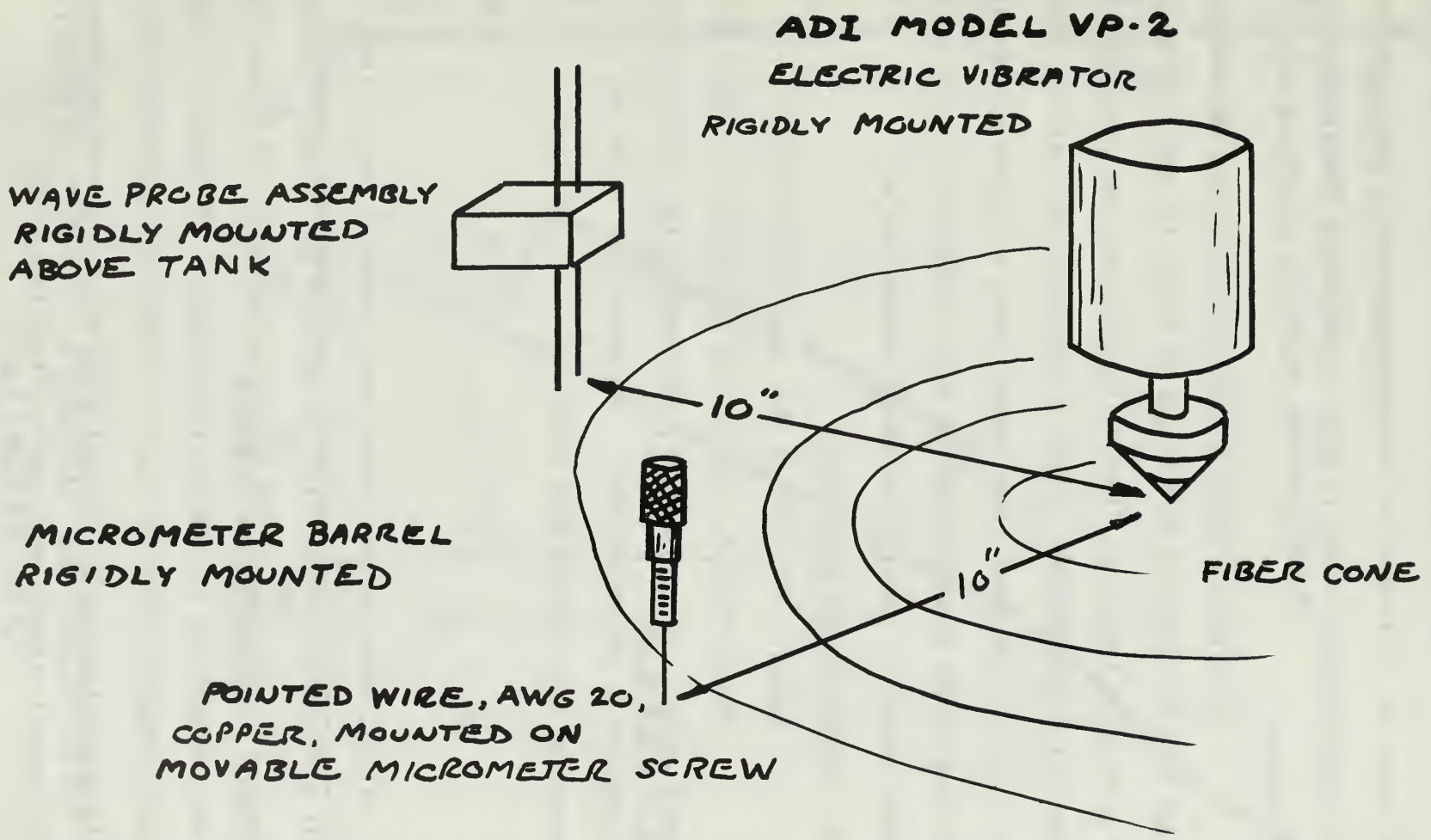

FIGURE 8. WAVE STAFF CALIBRATION, $8.0 \leq f \leq 30.0$ Hz

3. Capillary height (crest-to-trough) was then computed as being twice the difference in the two measurements. This step assumes that crest-to-trough height is equal to twice the value of mirror-to-crest height.

The crest-to-trough voltage variation from the wave staff was divided into the measured wave height to obtain the staff calibration at that particular frequency. This calibration was then normalized by dividing by the static calibration. Figure 9 summarizes the staff calibration from zero to 30 Hz. The error flags become larger at higher frequencies, because wave height decreases rapidly with increasing f, while the absolute possible error is a constant of the micrometer scale.

2. Processing the Wave Record

a. Temporal Variation of Mean Squared Wave Height

The correlator, as wired and programmed in figure 10, accepted the wave record, z(t), squared it, and averaged the resulting product for 20 seconds on a continuous basis. The correlator output was a voltage representing mean squared wave height, σ^2.

$$\sigma^2 = \frac{1}{20} \int_0^{20\ \text{sec}} z^2(t)\, dt = \left\langle z^2 \right\rangle$$

This voltage, displayed on a strip chart, revealed that σ^2 itself was itself a function of time, $\sigma^2(t)$, in spite of the 20 second integration; variations on the order of 20% were observed over a ten minute interval and were present for all wind-driven surfaces. The nature of these low-frequency temporal variations was not known; they appeared to be statistical, but on the possibility that there might have been an external cause, several attempts were made to study this effect.

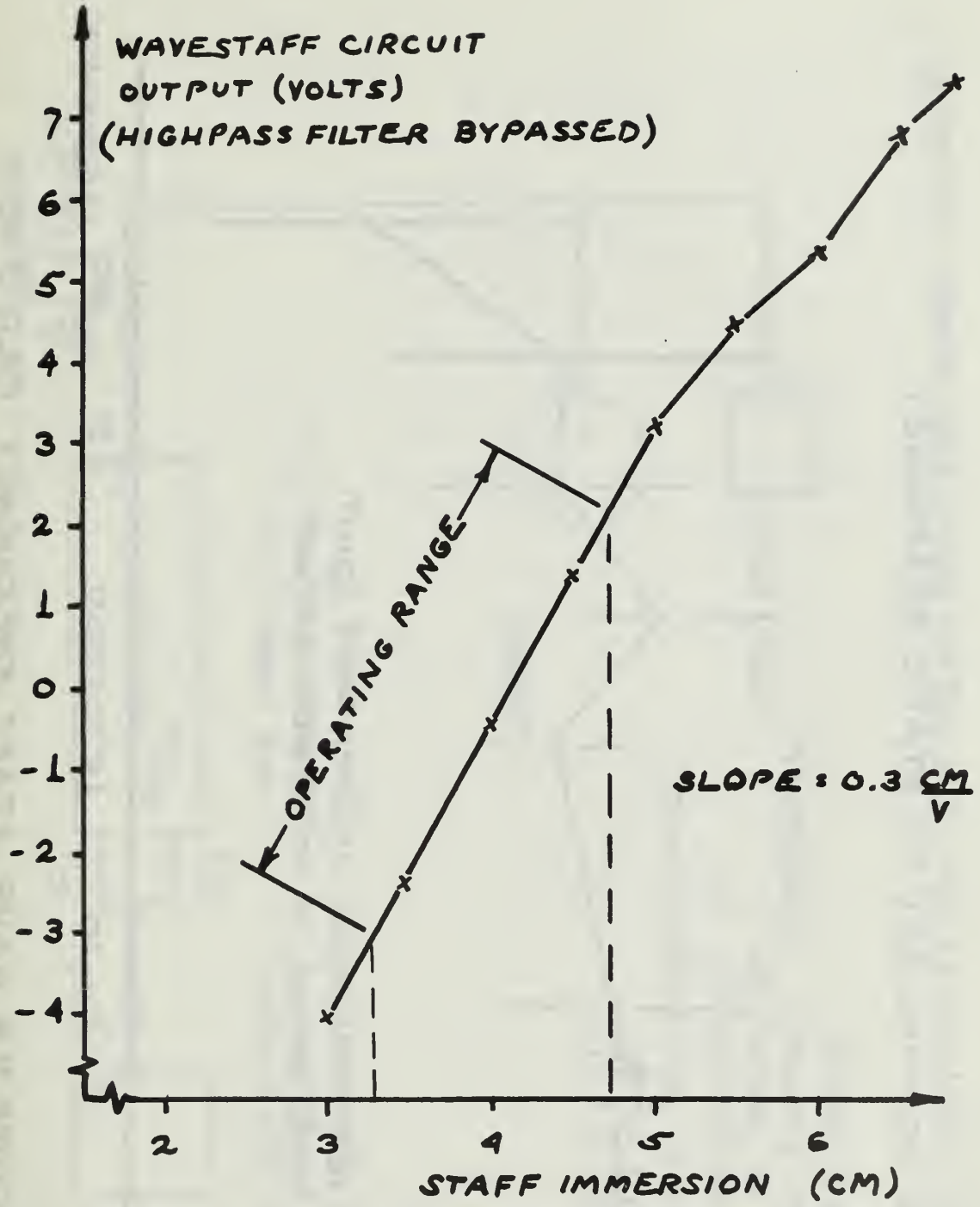

FIGURE 9A - STATIC WAVESTAFF CALIBRATION

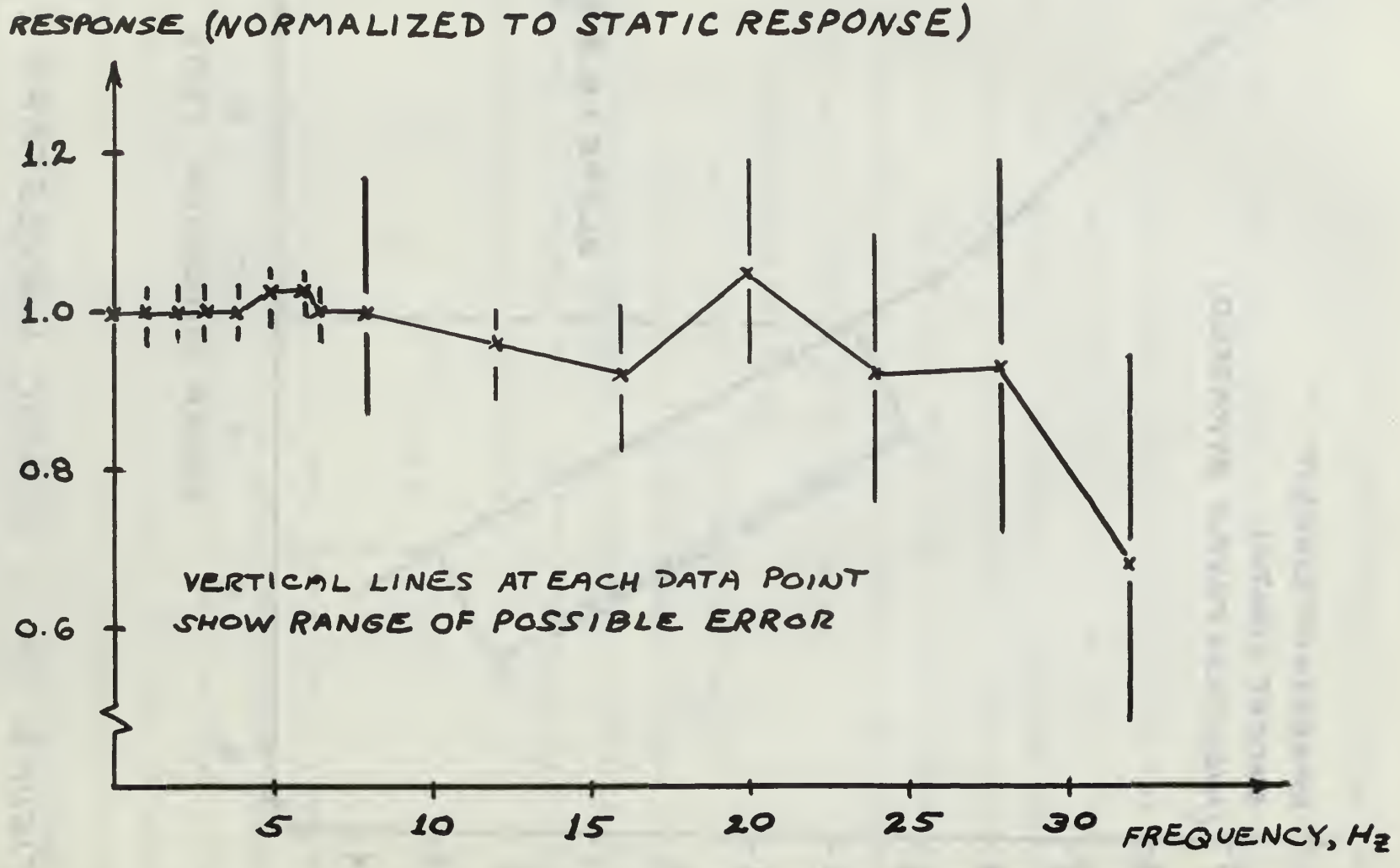

FIGURE 9B, WAVE STAFF FREQUENCY RESPONSE

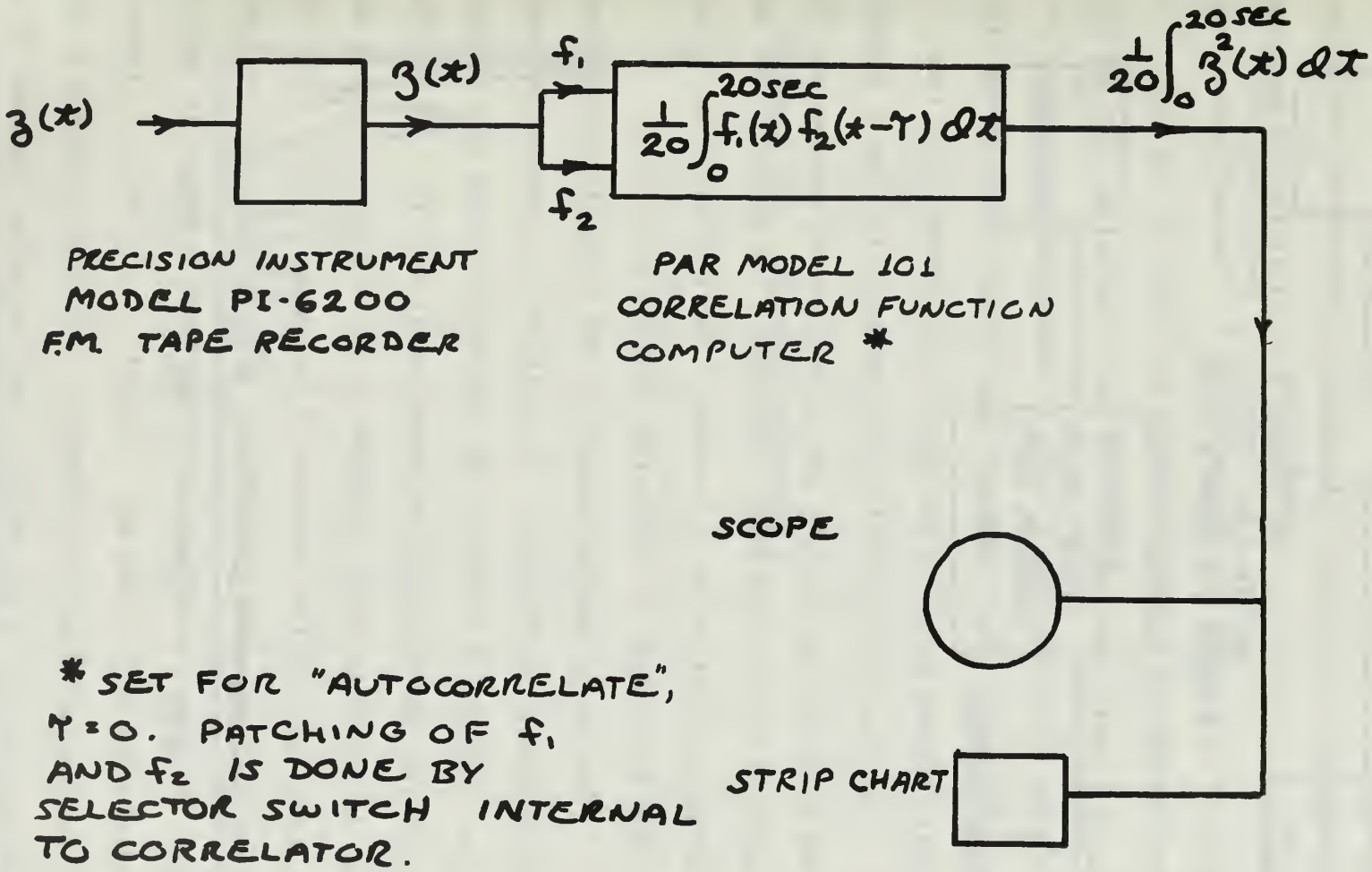

FIGURE 10. COMPUTATION OF MEAN SQUARED WAVE HEIGHT

Close examination of the strip chart revealed that the fluctuations in $\sigma^2(t)$ were of very low frequency, apparently less than 0.1 Hz (this observation being consistent with the 20 second time constant of the correlator). The possibility that the fluctuations were being introduced in the electronics was checked by oscillating the wave staff in a beaker of tank water as shown in figure 7. The amplitude of the oscillatory motion was a known constant; the resulting function, σ^2, when displayed on a strip chart was also constant, indicating that the previously observed variations were a real, if unexplained, phenomenon of the wind driven surfaces. The electrical power drawn by each of the five centrifugal fans was monitored and found to be constant with time.

As a second possibility, the period of the tank's natural seiche was determined by shocking the system (quickly opening and closing the large drain valve at the tank's west end). The period of the resulting water surface oscillation was 3.7 seconds — at least one order of magnitude smaller than the periods of fluctuation observed in $\sigma^2(t)$.

The energy spectral density of the fluctuations was determined using the equipment of figure 11. To shift the low frequencies into a range more tractable to analysis, the function $\sigma^2(t)$ was tape recorded at speed 0.375 IPS, and replayed for processing at 37.5 IPS. It was found necessary to eliminate the DC component of the signal, since this would produce delta function-like behavior at f=0 on the spectrum plot, possibly masing the low frequencies of interest. DC elimination was done with a high-pass, RC filter, whose parameters are shown in figure 11. The surviving signal after this filter was $\sigma^2(100t^*) - \sigma^2(100t^*)$, (where t^* = time in the playback frame of reference). The autocorrelation of this function was computed by the PAR-101, then the cosine transform of the

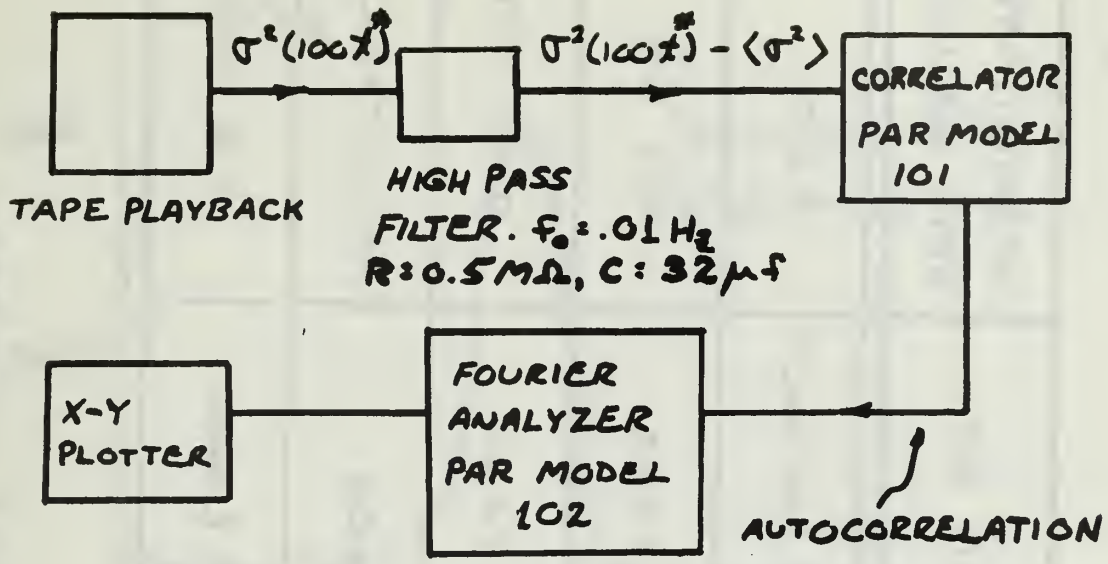

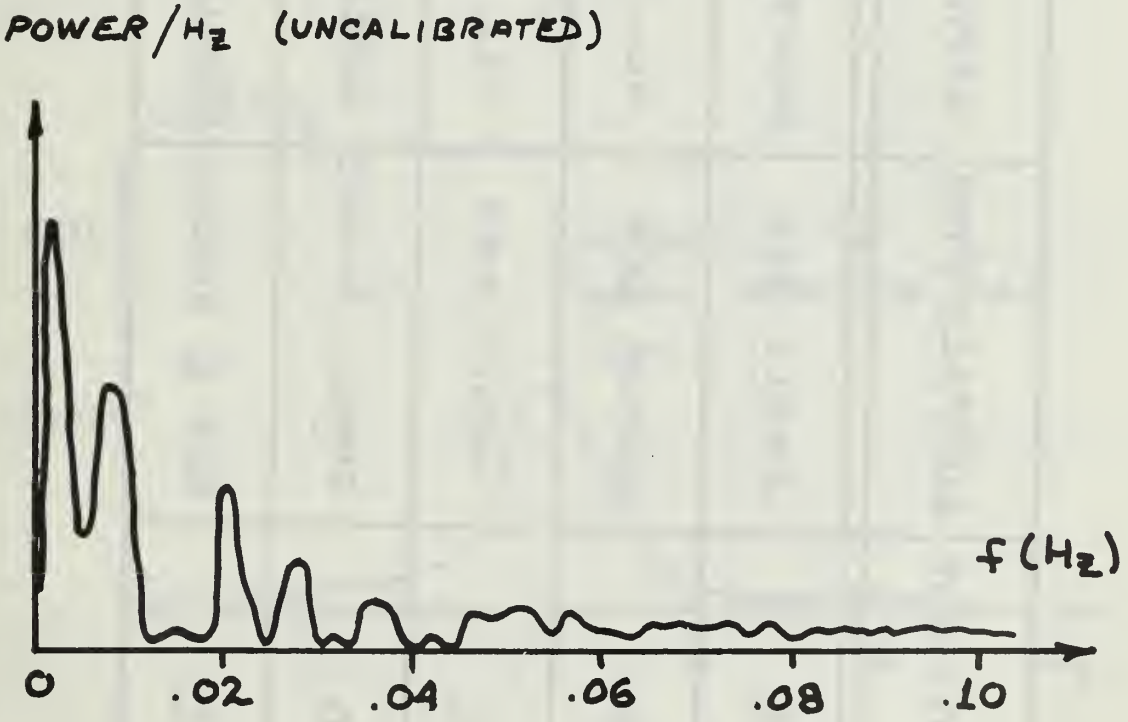

FIGURE 11 POWER SPECTRAL DENSITY OF $\sigma^2(t)$

Wave Tank
50:1 Scale

DESIGNATOR	SURFACE TYPE	GENERATED BY:	APPROXIMATE RMS HEIGHT
A	SMALL SEA	BACK CENTER FAN ONLY	0.1 CM
B	MEDIUM SEA	ALL BACK FANS	0.2 CM
C	HEAVY SEA	ALL FIVE FANS	0.45 CM
D	SWELL ALONE	SWELLMAKER	ADJUSTABLE
E	SEA & SWELL	SWELLMAKER & BACK FANS	0.2 CM

FIGURE 12. WATER SURFACES CHOSEN

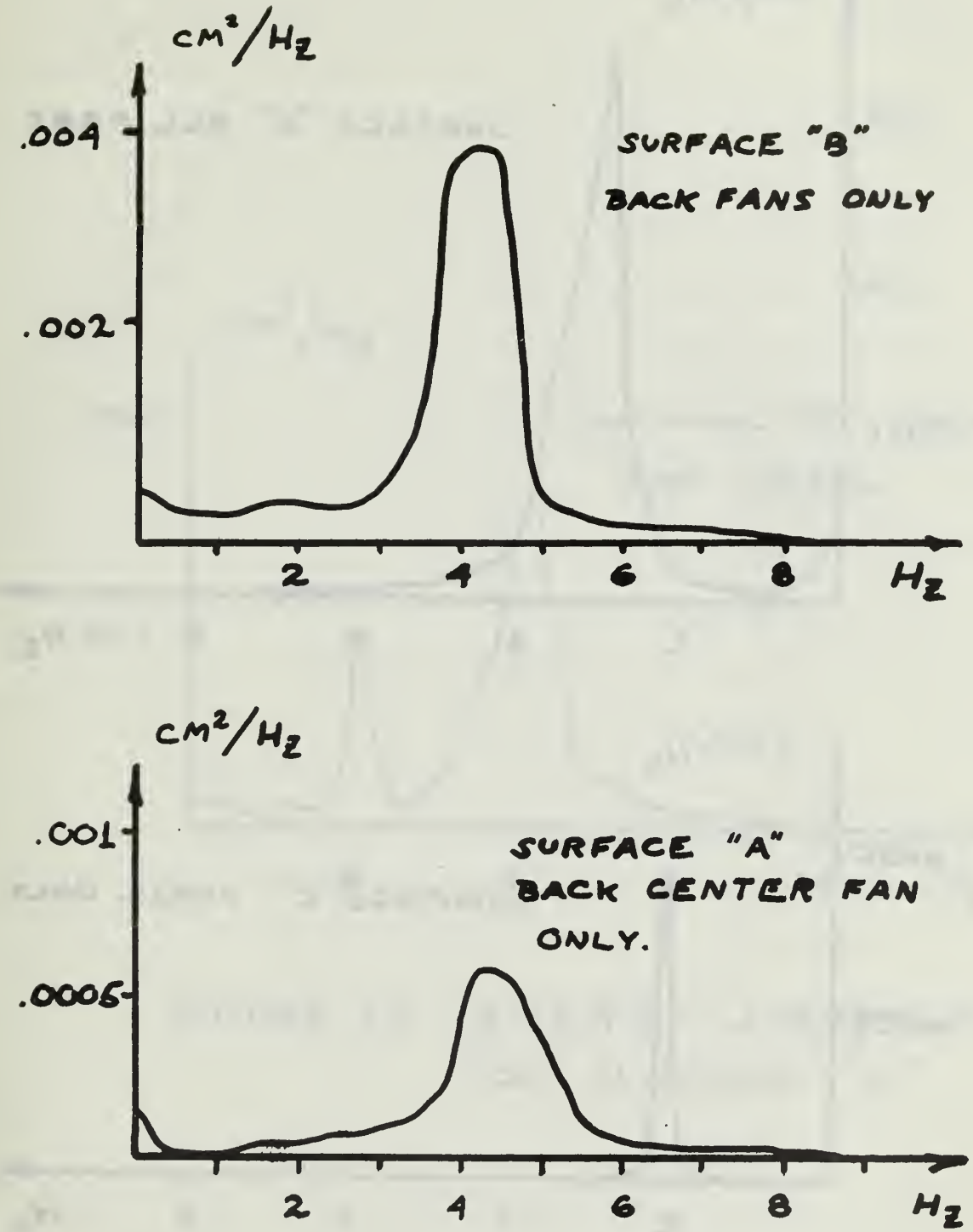

FIGURE 13. ENERGY SPECTRA FOR SURFACES "A" AND "B"

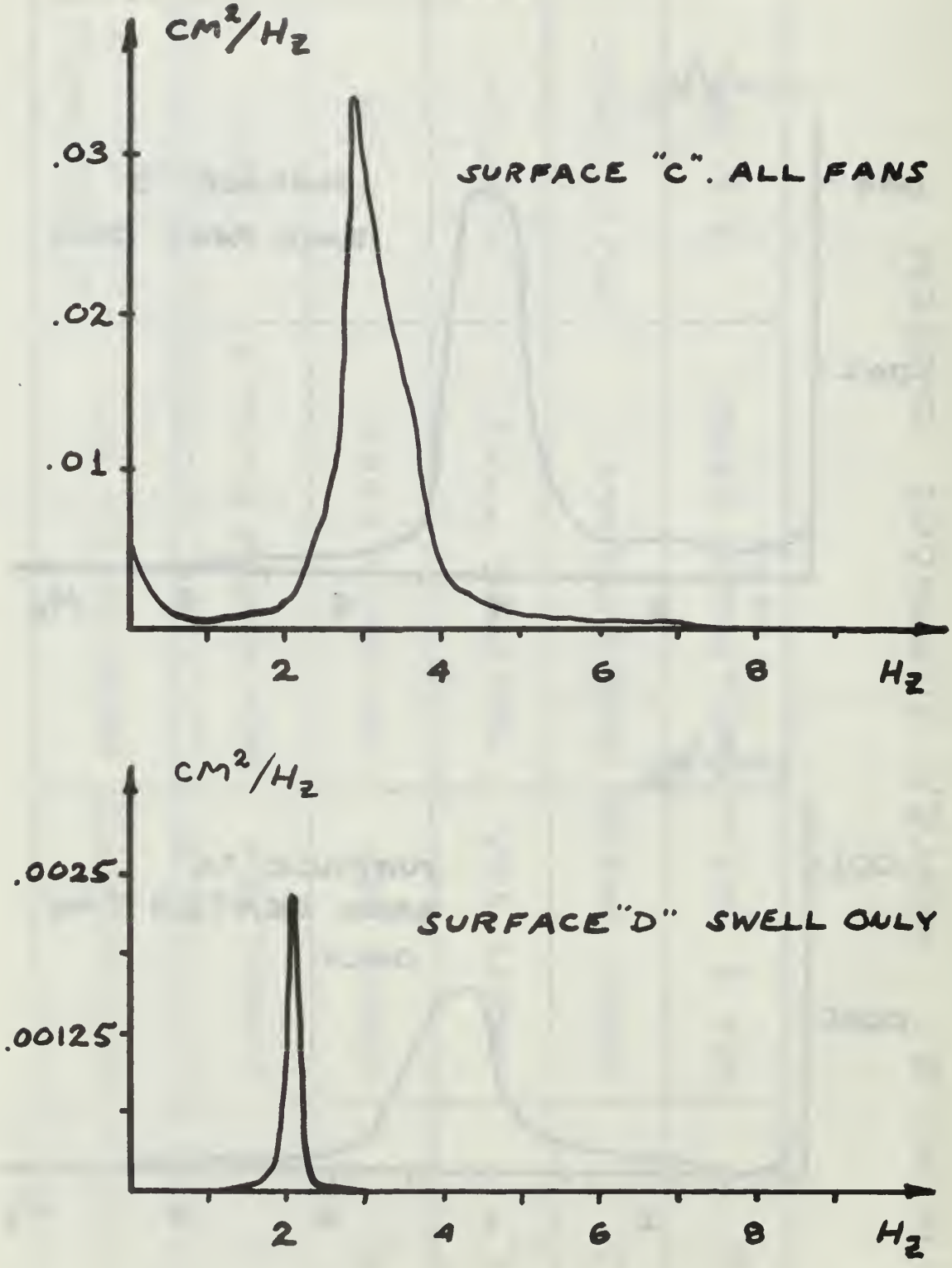

FIGURE 14. ENERGY SPECTRA FOR SURFACES "C" AND "D"

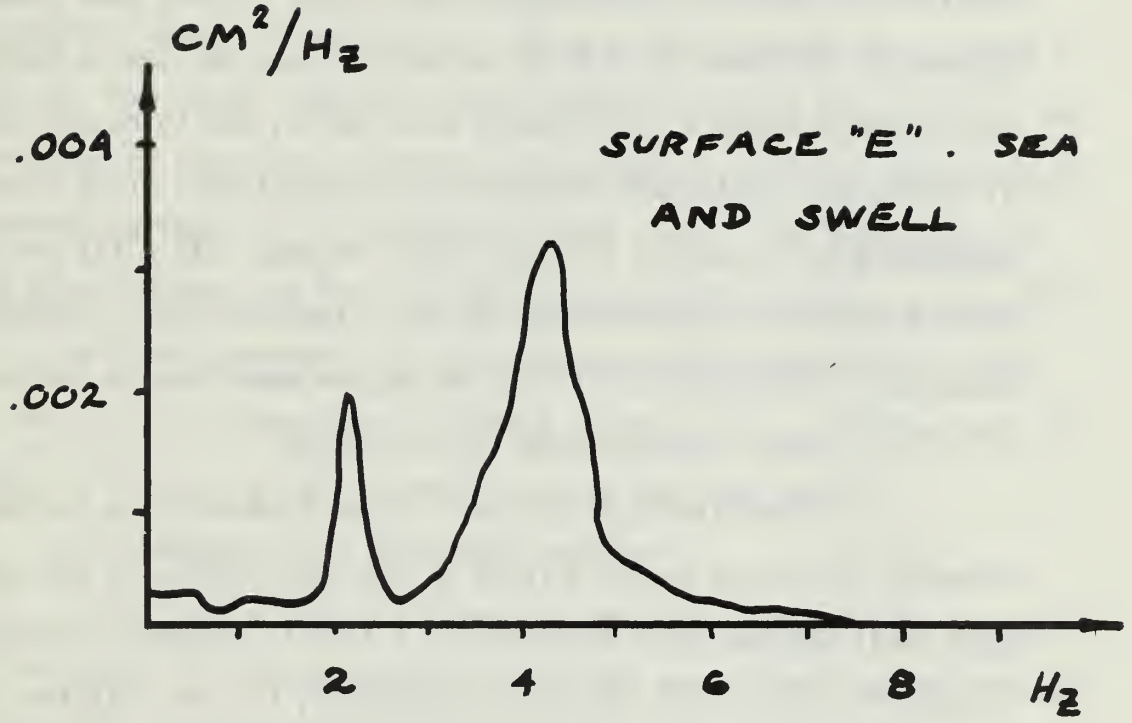

FIGURE 15. ENERGY SPECTRUM FOR SURFACE "E"

autocorrelation was determined by the PAR-102, which yielded the energy spectral density in accordance with the Weiner-Kinchine Theorem.

The resulting plot, shown in figure 11, revealed three strong, low-frequency components with periods of approximately 500, 100 and 50 seconds. It is possible that these components might have been introduced by the high-pass filter, but it is believed that the fluctuations are statistical, possibly introduced by non-linear surface wave interaction. Because of the behavior of this variable, it was decided to monitor it continuously during all scattering experiments, and to record its value at the instant that sound scattering data were taken. This procedure appeared both reasonable and consistent, because both $\sigma^2(t)$ and the scattered sound data were processed through integrators with identical time constants. The mechanics of data taking are described in section III-D.

b. Water Surfaces Used for Scattering

Five water surfaces were chosen from which to scatter sound, covering the widest possible range of RMS wave height, σ, and containing both swell and sea-swell combination; a tabular summary of these surfaces is given in figure 12. Using the correlator, Fourier analyzer, and plotter (but not the filter) of figure 11, energy spectral density plots were made for the surfaces and are presented in figures 13 through 15. For consecutive runs under identical wind source conditions, slight shifting of peak size and location was always noted, as well as changes in the total area under the curve, a fact previously established since area under the curve is equal to mean squared wave height, $\sigma^2(t)$. Figures 13 through 15 are representitive energy spectra, each compiled from examination of several spectra for nominally the "same" statistical surface. It should be noted that nonlinear interaction caused the sea and swell

spectrum "E" to be significantly different from superposition of the two constituent spectral (sea "B" and swell "D").

A closer analysis of the energy spectral density of wind driven sea "B" was made by plotting the data on log-log axes. A continuous, four hour wave record, z(t), was tape recorded, and replayed at one-hundred-times speed, z(100t*), into a General Radio Wave Analyzer, model 1900-A, using a bandwidth of 3 Hz; the data obtained are plotted in figure 16. The curve labelled "noise" represents total system noise, and was obtained by frequency analyzing a four hour tape of the "wave record" of a mirror surface, in the manner described above. The dependence of energy upon frequency at the high-frequency dropoff was found to be $f^{-4.8}$, which is in close agreement with the Neumann-Pierson spectrum for wind waves and Phillips theory [Ref. 6] which predicts f^{-5}. Scheible [Ref. 3] obtained $f^{-5.5}$ for a slightly smaller sea in the same tank.

c. Inhomogeneity of the Water Surface

The wind driven seas produced were not statistically homogeneous. The degree of non-homogeneity in the RMS wave height was determined by analysis of 30 minute wave records from the nine surface locations shown in figure 17. A wave record from any one of the nine locations was processed as shown in figure 10. The output of the correlator was a 30-minute record of $\sigma^2(t)$, which was tape recorded at .375 IPS. This record was then replayed at 3.75 IPS into the analogue-to-digital converter of the SDS 9300 digital computer. The converter sampled the input function, $\sigma^2(10t^*)$, at a 30 Hz rate. The square root of each sample was then extracted, which resulted in an ensemble of approximately 5400 digital values of the RMS wave height, σ. The mean and standard deviation were computed for each of the nine ensembles, and the results are presented in

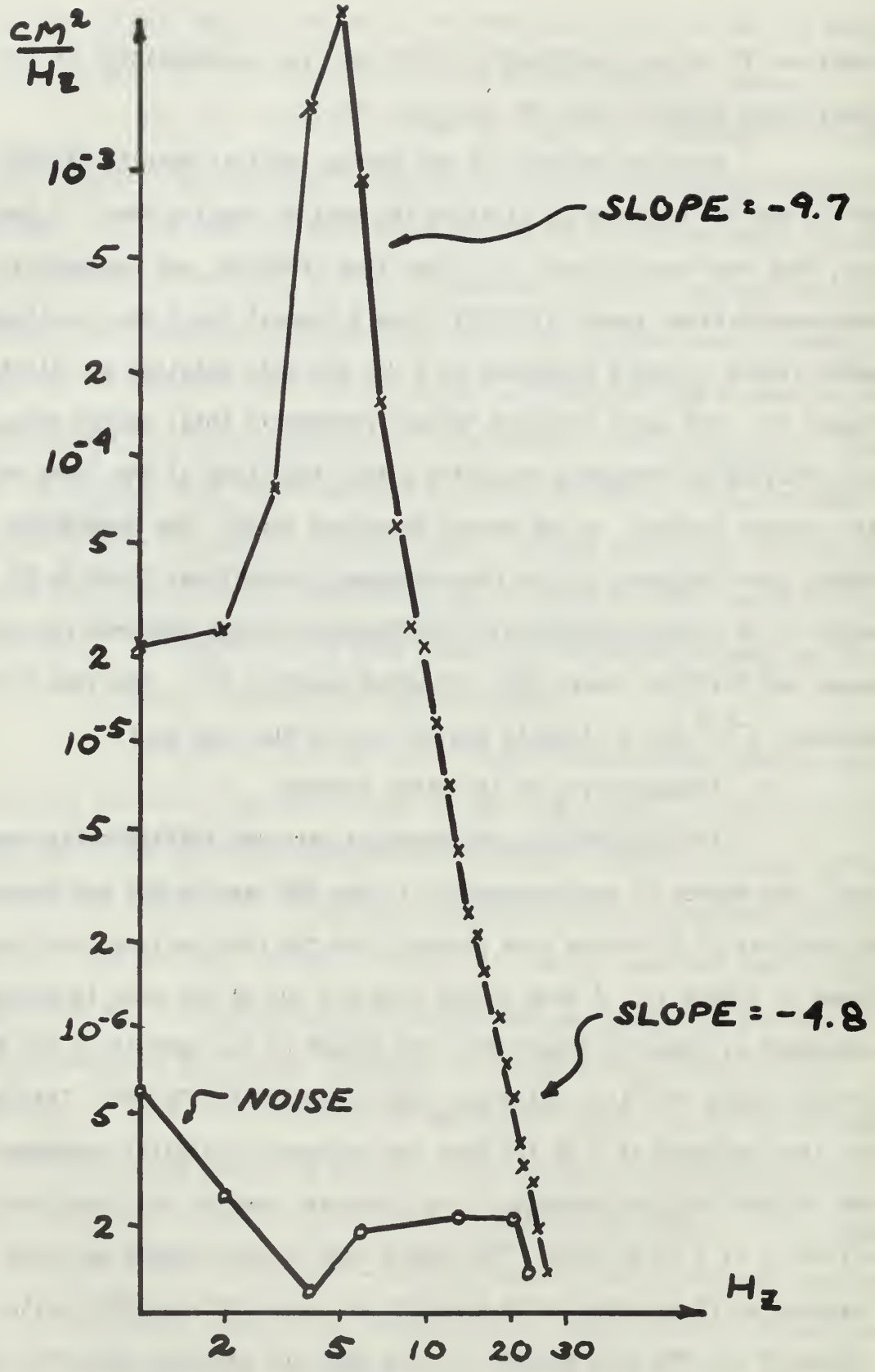

FIGURE 16. ENERGY SPECTRUM OF SEA "B"

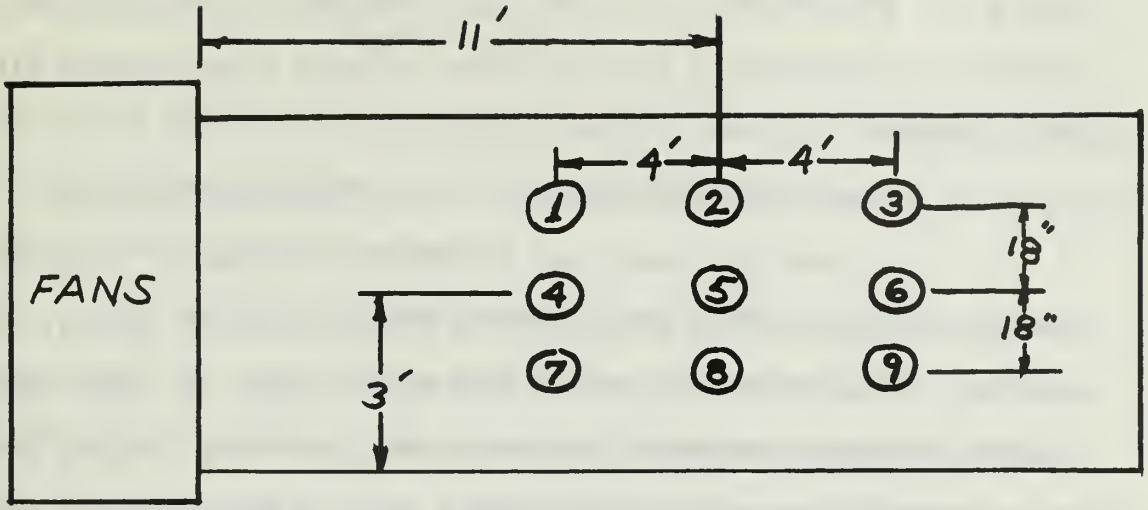

	RMS WAVE HEIGHT	
LOCATION	MEAN	STD DEVIATION
1	.232	.010
2	.273	.019
3	.327	.024
4	.209	.010
5	.266	.017
6	.295	.026
7	.234	.013
8	.256	.015
9	.346	.021

FIGURE 17 INHOMOGENEITY OF THE RMS WAVE HEIGHT OF WIND DRIVEN SURFACE "B"

figure 17. Wind driven sea "B" was used throughout; a fetch-limited situation is indicated by the significant increase of wave height with fetch distance.

d. Wave Height Distributions for the Scattering Surfaces

As previously mentioned in section II-A, the e^{-g} term for coherent specular scatter was derived by Beckmann (and all others) after assuming a Gaussian distribution of wave heights [Ref. 2]. Wave height distributions were determined for the various scattering surfaces and are presented in Appendix B, along with a detailed description of how the data were obtained. In summary of this appendix, it can be stated that all wind driven seas — including the sea-swell combination — had height distributions which resembled the Gaussian, although all were skewed to the right. The pure swell, however, had a height distribution which resembled that of a sine wave.

C. ANALYSIS OF THE SCATTERED SOUND PRESSURE

Continuous-wave, rather than pulsed, sound was used in the scattering study; however, at each frequency and for each transducer position, pulsed sound was used to determine the magnitude of the unwanted direct ray between sender and receiver, as well as other non-surface reflections. In most cases the ratio of direct-path to mirror-reflected pressure was about .01, and in no case did it exceed .03. Unwanted reflections from the tank walls were generally one order of magnitude smaller than the direct path signal.

1. Isolating the Coherent, Received Sound Pressure

It was assumed that the sound pressure, p, received at the hydrophone after rough surface reflection was composed of two components, one coherent with the transmitted signal and the other incoherent.

$$p = p_{coh} + p_{incoh}$$

Use of the PAR Correlation Function Computer made possible the isolation of the coherent component, and (in principle) determination of the magnitude of the incoherent component.

The acoustic pressure corresponding to the driving voltage was represented by $p_d(t) = P_d \cos(\omega t)$. When the surface was in the mirror condition, the output of the receiving hydrophone was totally coherent with the sent signal. After amplification this received signal was represented by $BP_d \cos \omega(t-t')$, where B is an amplitude scale factor, and $\omega t'$ represents the phase shift due to propagation distance and possible phase shifts within the transducers. Cross-correlation of sent and received signals produced the function $M(\tau)$.

$$M(\tau) = \frac{B}{20} \int_0^{20\ \text{sec}} P_d^2 \cos \omega(t-\tau) \cos \omega(t-t')\, dt$$

where τ = correlation delay applied to the $p_d(t)$ input.
The output of the correlator was displayed on an oscilloscope, from which the value of $M(\tau)$ could be read as a function of the variable τ. The function has a maximum at $\tau = t'$.

$$M_{max} = M(t') = \frac{B}{20} \int_0^{20\ \text{sec}} P_d^2 \cos^2 \omega(t-t')\, dt$$

$$= B P_d^2 \cos^2(\omega t - \omega t') = B \left\langle p_d^2(t) \right\rangle = B \quad I_d$$

I_d is proportional to driving intensity, and $\langle\ \rangle$ means an average over 20 seconds.

The water surface was then roughened and the correlation repeated, taking care not to change the driving pressure, $p_d(t)$. The scattered pressure was now of the form

$$p = ABP_d \cos\ (t-t') + p(t)_{incoh}$$

where A = amplitude reduction factor due to rough surface. Cross-correlation of sent and received signals then gave $N(\tau)$, which was composed of two integrals.

$$N(\tau) = \frac{AB}{20} \int_0^{20\ sec} P_d^2 \cos \omega(t-t') \cos \omega(t-\tau)\ dt \quad +$$

$$\frac{P_d}{20} \int_0^{20\ sec} p(t)_{incoh} \cdot \cos \omega(t-\tau)\ dt$$

The second term vanishes because of the incoherence of the two factors in the integrand. The first term has a maximum at $\tau = t'$.

$$N_{max} = N(t') = \frac{AB}{20} \int_0^{20\ sec} P_d^2 \cos^2 \omega(t-t')\ dt$$

$$= AB\ \ p_d^2(t) = AB \left\langle I_d \right\rangle$$

Forming the ratio of N_{max} to M_{max} gives:

$$\left.\frac{N(\tau)}{M(\tau)}\right|^{\tau=t'} = \frac{AB \left\langle I_d \right\rangle}{B \left\langle I_d \right\rangle} = A$$

Since A relates pressures, the intensities are related by A^2:

$$\left\langle \frac{I(coh)}{I(mirror)} \right\rangle = A^2$$

where $\left\langle I_{coh} \right\rangle = \left\langle p_{coh} p^*_{coh} \right\rangle$ and $I_{mirror} = B^2 I_d$

The theory of section II-A predicts that $A^2 = e^{-g}$.

2. The Incoherent Component of Scattered Sound Pressure

In principle at least, the ratio of incoherent to mirror intensity

can be determined using the correlator in both the auto and cross-correlation modes. The error calculation of Appendix A, however, shows that for small values of g the uncertainty involved in such a procedure makes the result almost meaningless; this situation evolves because the computation requires the subtraction of two nearly equal numbers, each with non-trivial relative error. Although not used for computation the method is outlined briefly below.

With mirror surface, the received sound pressure is, as before, $BP_d \cos \omega(t-t')$. Autocorrelation of this signal yields $C(\tau)$:

$$C(\tau) = \frac{B^2 P_d^2}{20} \int_0^{20\ \text{sec}} \cos \omega(t-t') \cos \omega(t-t'-\tau)\ dt$$

This function has a maximum at $\tau = 0$, equal to

$$C(\tau)_{max} = C(0) = \frac{B^2 P_d^2}{20} \int_0^{20\ \text{sec}} \cos^2 \omega(t-t')\ dt = B^2\ I_d$$

The surface is roughened and the autocorrelation repeated; the received signal is $ABP_d \cos \omega(t-t') + p(t)_{incoh}$, and its autocorrelation, evaluated at $\tau = 0$ is $D(\tau)|^{\tau=0}$.

$$D(0) = \frac{A^2 B^2 P_d^2}{20} \int_0^{20\ \text{sec}} \cos^2 \omega(t-t')\ dt$$

$$+ \frac{2ABP_d}{20} \int_0^{20\ \text{sec}} p(t)_{incoh} \cos \omega(t-t')\ dt$$

$$+ \frac{1}{20} \int_0^{20\ \text{sec}} p^2(t)_{incoh}\ dt$$

The second term vanishes upon integration; the remaining two terms are:

$$D(0) = A^2 B^2 \left\langle I_d \right\rangle + \left\langle I_{incoh} \right\rangle$$

Forming the ratio $D(0)/C(0)$ gives a new quantity R:

$$R \quad \frac{D(0)}{C(0)} = \frac{A^2B^2 \left\langle I_d \right\rangle + \left\langle I_{incoh} \right\rangle}{B^2 \left\langle I_d \right\rangle} = A^2 + \frac{\left\langle I_{incoh} \right\rangle}{B^2 \left\langle I_d \right\rangle}$$

But $B^2 \left\langle I_d \right\rangle = \left\langle I(mirror) \right\rangle$

$$R = A^2 \frac{\left\langle I_{incoh} \right\rangle}{\left\langle I(mirror) \right\rangle}$$

$$\frac{\left\langle I_{incoh} \right\rangle}{\left\langle I_{mirror} \right\rangle} = R - A^2$$

Determination of both A^2 and R required the use of the correlator; since only one such instrument was available, the two quantities could not have been computed simultaneously, a fact which would have further added to total uncertainty in the final result.

D. DATA COLLECTION PROCEDURE

A data run consisted of the following steps performed in sequence:

1. With mirror surface and the transducers positioned at the desired grazing angle, the receiver and projector were physically aligned for maximum scattered return.
2. Using pulsed sound, the ratio of unwanted direct-path pressure to mirror-surface-reflected-pressure was determined and recorded. Only data with direct path less than 3.0% of mirror reflection value were studied.
3. With mirror surface and continuous-wave sound, the cross-correlation of driving voltage with received signal was measured; the value of the maximum of this function was read from an oscilloscope after 180 seconds of correlator computation time (corresponding to six time constants of the integrators).
4. The surface was then roughened, and the cross-correlation was repeated. The surface wave record, z(t), was tape recorded during this correlation, and the time of the correlation reading was marked by annotating the tape on a separate voice channel; duration of this record was three minutes.

5. At a later time the tape containing z(t) was replayed at original speed and autocorrelated with zero delay time. The resulting correlator output — mean squared wave height — was read and recorded when directed by the voice channel, corresponding to the time of previously having read sound correlation.

The circuitry and equipment used in the foregoing steps are shown in figures 18 through 20. A separate data sheet was filled out for each data run, and the run was identified by its most important parameters; an example of run labelling is given in figure 21.

Even though both RMS wave height and A^2 varied slightly with time throughout a data run (see section III-B-2-a) they were determined as nearly simultaneously as possible, each having been processed by integrators with the same time constant (the same integrators). It is believed that this method permitted the taking of meaningful data, the precision of which was not appreciably degraded by temporal variation of important parameters.

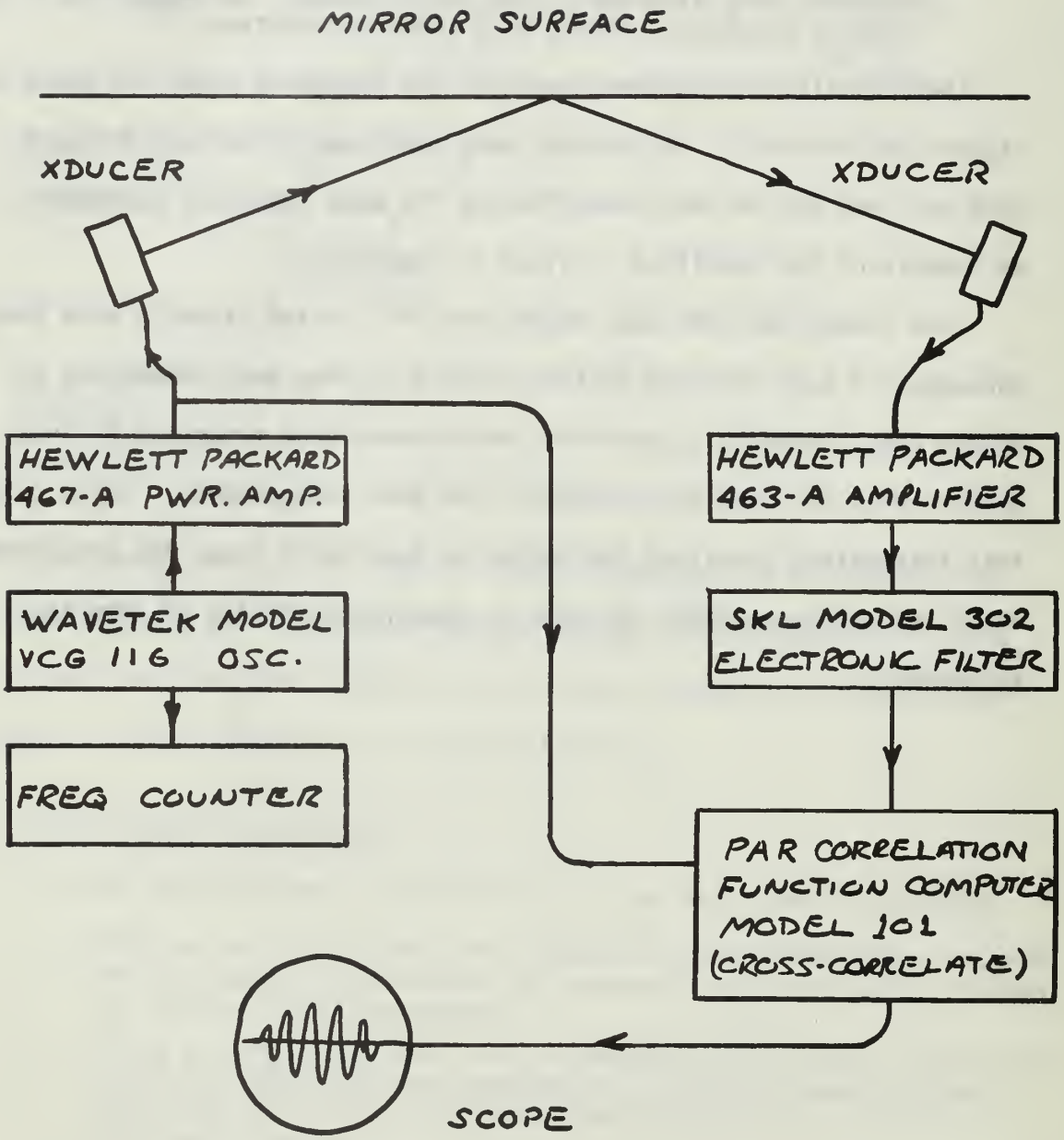

FIGURE 18 - MAKING A DATA RUN, OBTAINING MIRROR CORRELATION

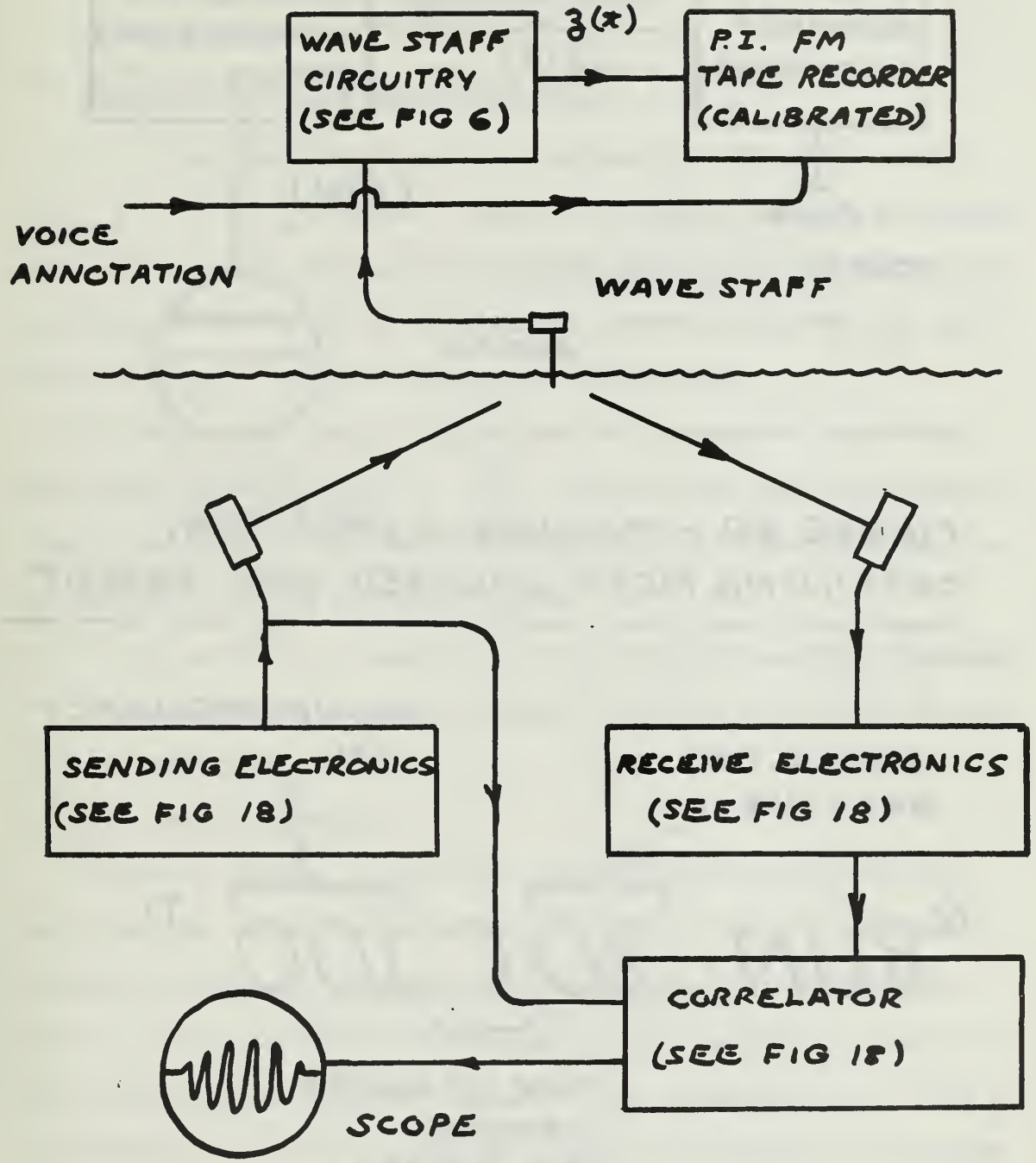

FIGURE 19 - MAKING A DATA RUN, OBTAINING ROUGH-SURFACE CORRELATION

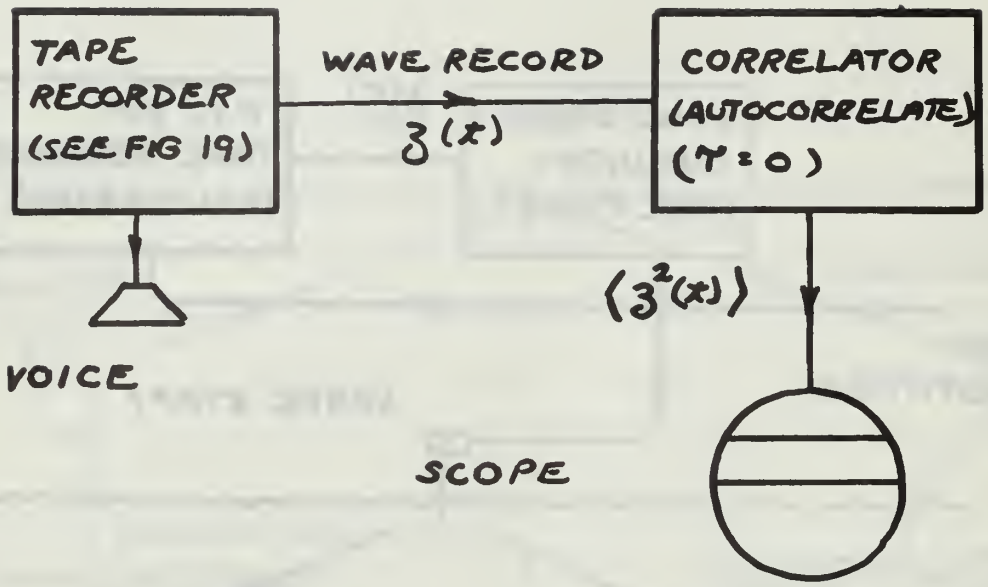

FIGURE 20 - MAKING A DATA RUN, OBTAINING MEAN SQUARED WAVE HEIGHT

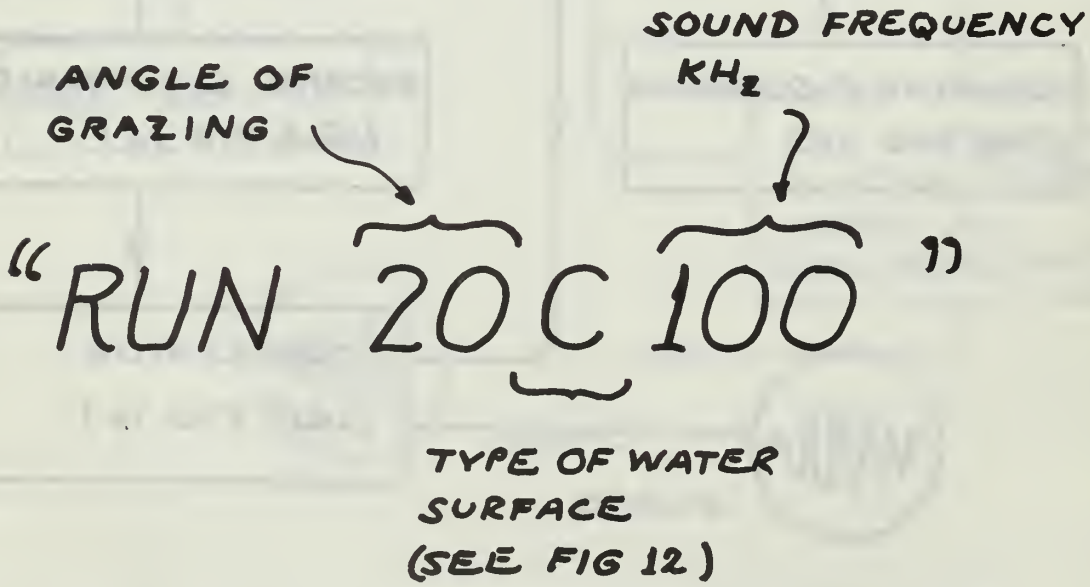

FIGURE 21 - IDENTIFICATION OF DATA RUNS

IV. ANALYSIS OF DATA

A. DEPENDENCE OF COHERENT, SPECULAR SCATTER ON SURFACE ROUGHNESS FOR SIMPLE AND COMPOUND SEAS

If surface shadowing is neglible, Beckmann and all others predict $\langle I_{coh} \rangle = e^{-g} I_{mirror}$ (Eq. 1). There is no reason, however, to believe that this function, derived for a Gaussian distribution of wave heights, would govern the scattering of specular, coherent sound from pure swell with its almost sinusoidal wave record (Appendix B).

To compare experimental observations with theoretical predictions, the ratio $\left\langle \frac{I_{coh}(obs)}{I_{coh}(predict)} \right\rangle = \frac{A^2}{e^{-g}}$ was formed for each data observation. Departures of this ratio from unity can be attributed to one, or a combination, of the following factors:

1. Non-validity of equation 1 in predicting the observed phenomenon.
2. Experimental uncertainty (shown in Appendix A to be 27% for the worst case).
3. Surface shadowing.

Figures 22 through 25 show this quantity plotted against grazing angle for the various scattering surfaces. In all cases — with the exception of figure 23 — the ratio $\left\langle \frac{I_{coh}(obs)}{I_{coh}(predict)} \right\rangle$ is within 8% of unity, well inside the worst case experimental uncertainty. Figure 24 shows that coherent, specular scattering from narrow-band swell alone is predicted by e^{-g} with at least the degree of precision found when the sea has a Gaussian distribution of wave heights.

The curve representing 100 kHz and wind driven surface "C" shows a marked and significant departure from predicted behavior in the vicinity of 20° grazing angle. Three identical data runs were made on different days at 20° grazing to check the phenomenon's reproducibility (Figure 23);

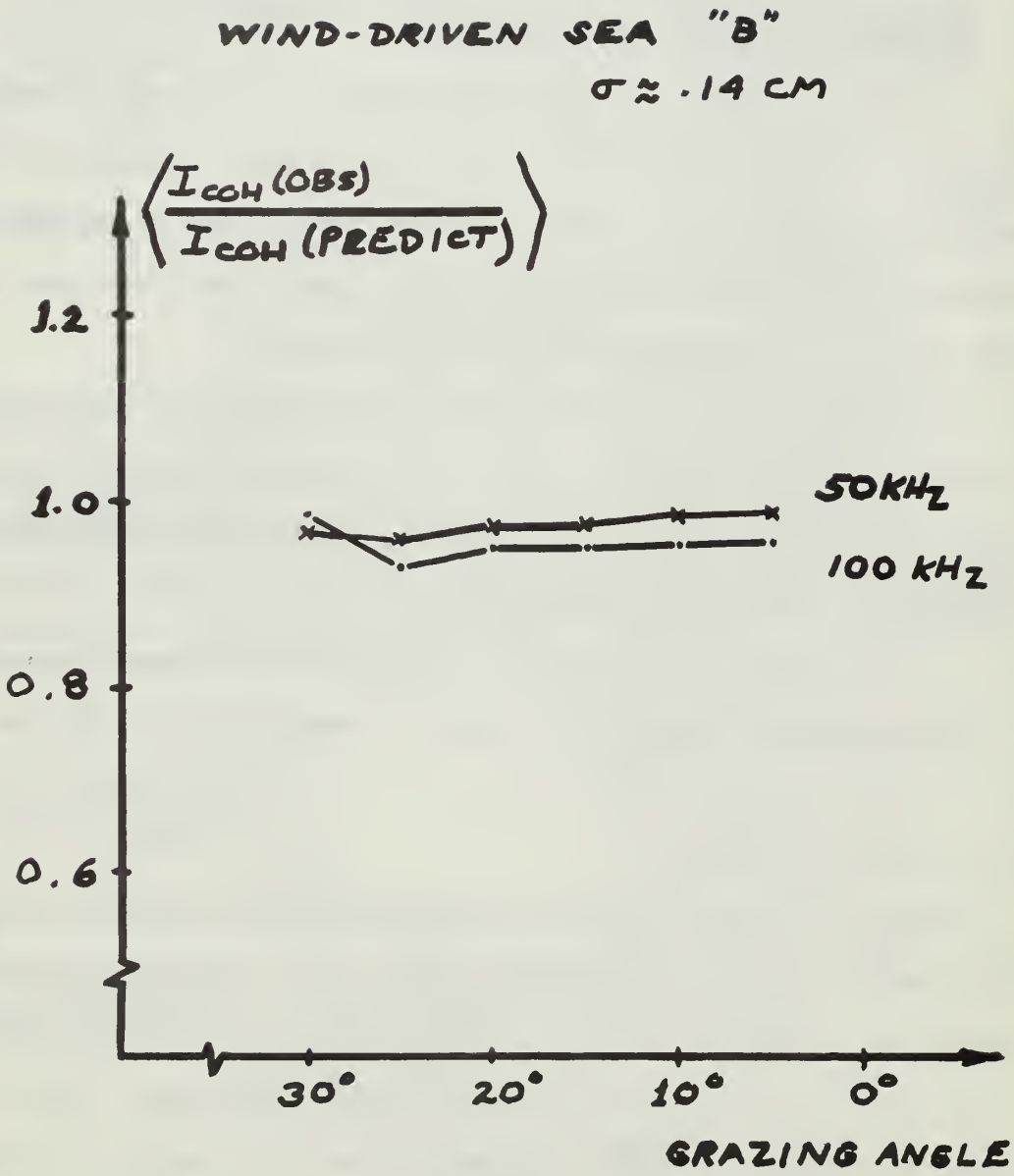

FIGURE 22 - WATER SURFACE "B"

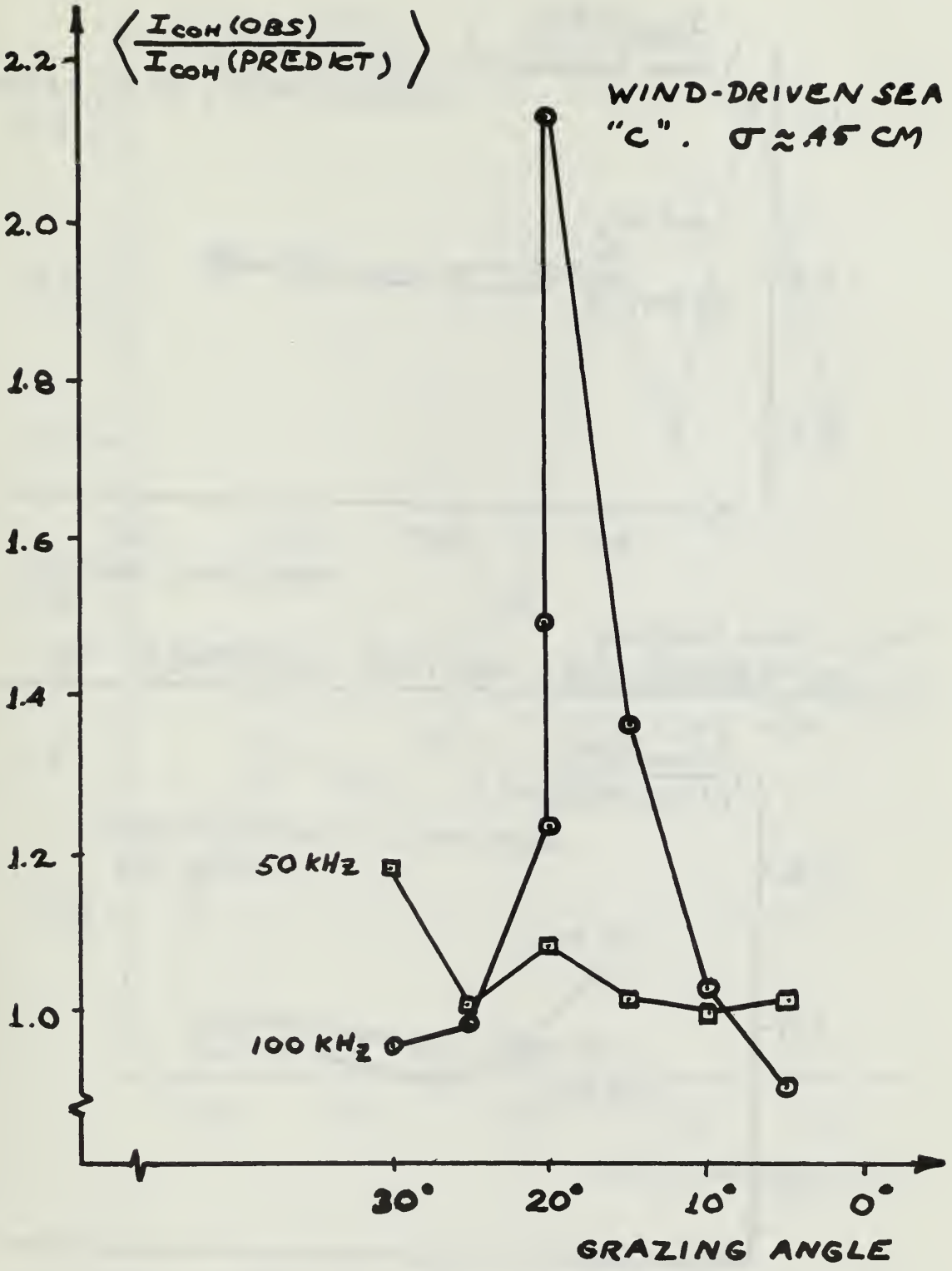

FIGURE 23 - WATER SURFACE "C"

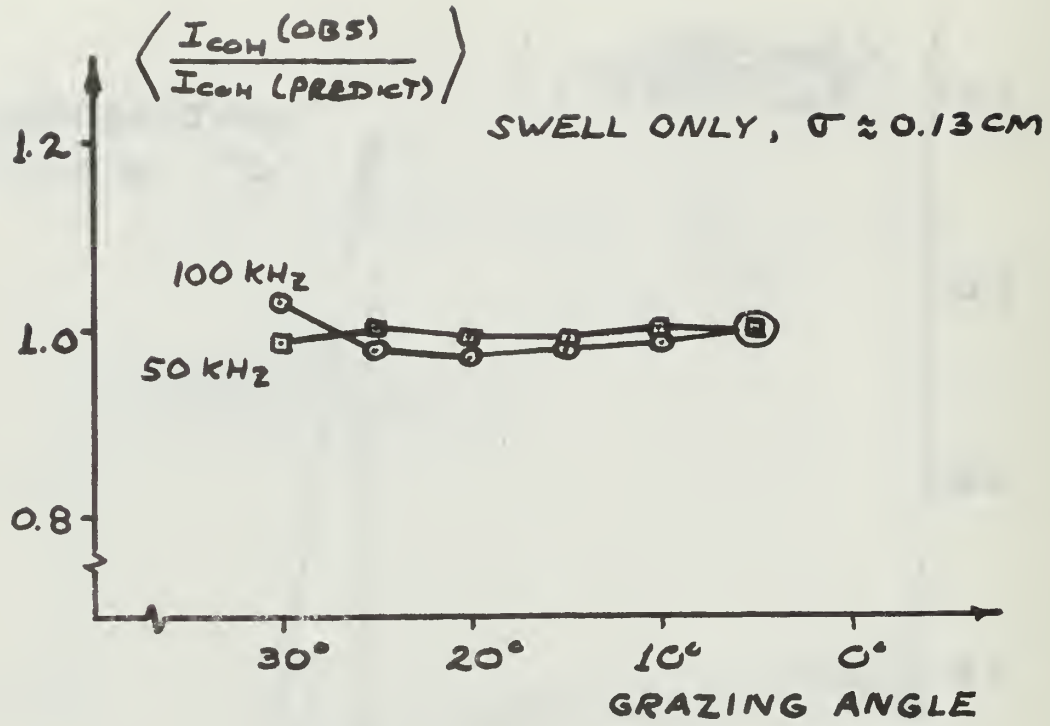

FIGURE 24 - WATER SURFACE "D"

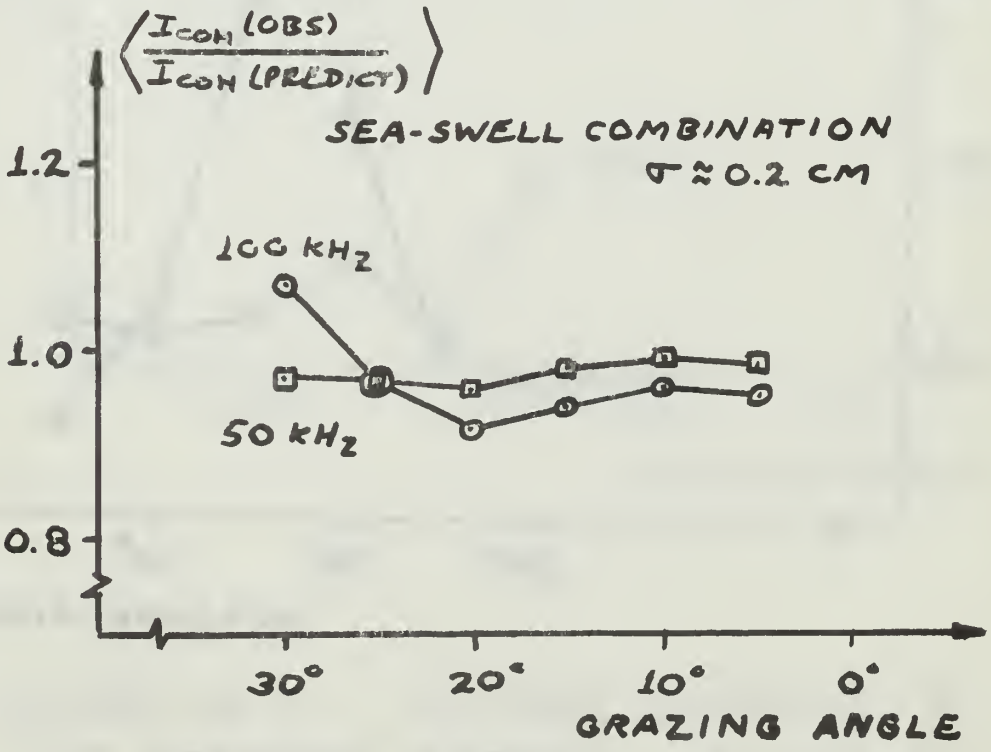

FIGURE 25 - WATER SURFACE "E"

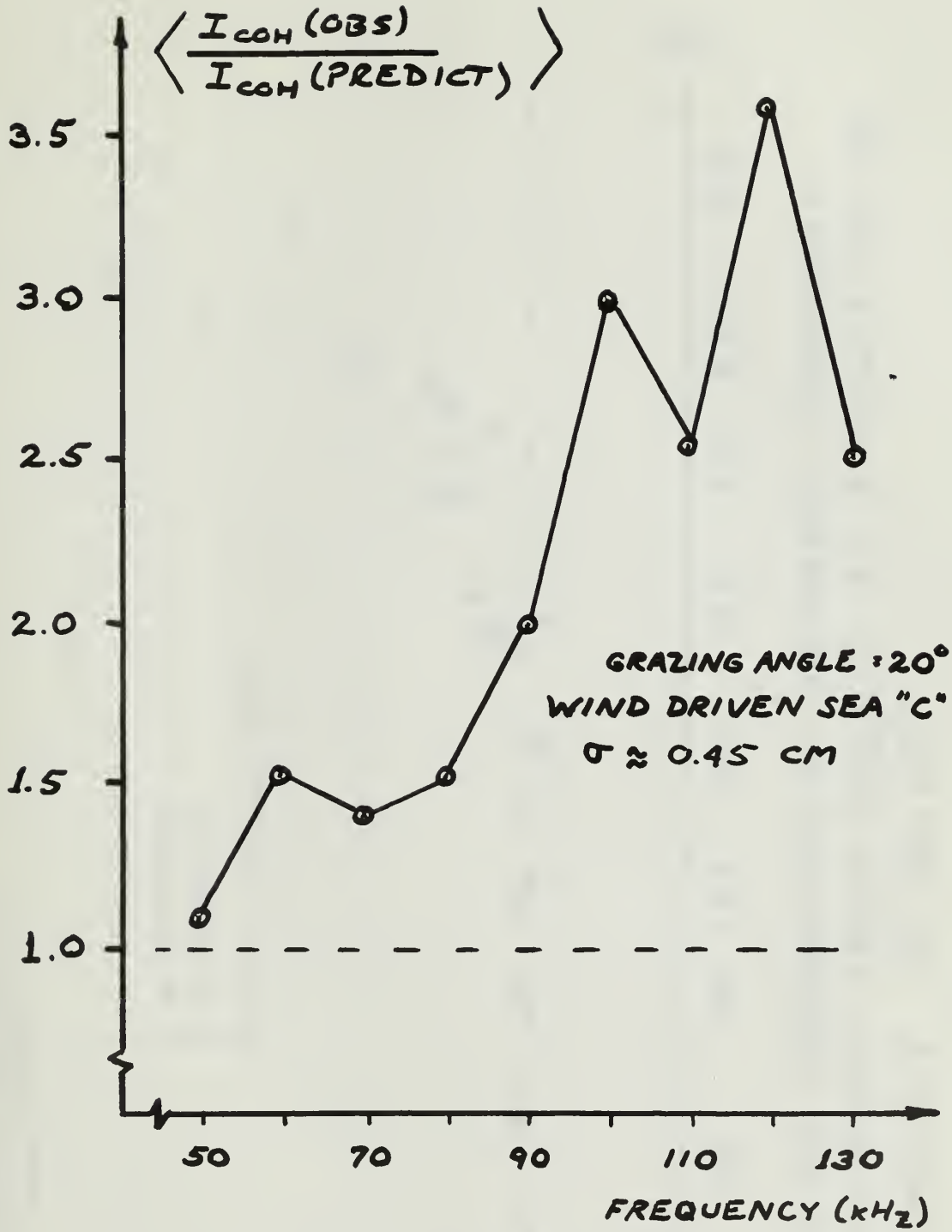

FIGURE 26 - DEPARTURE OF COHERENT COMPONENT FROM THEORY, AS A FUNCTION OF FREQUENCY AT $\Theta = 20°$.

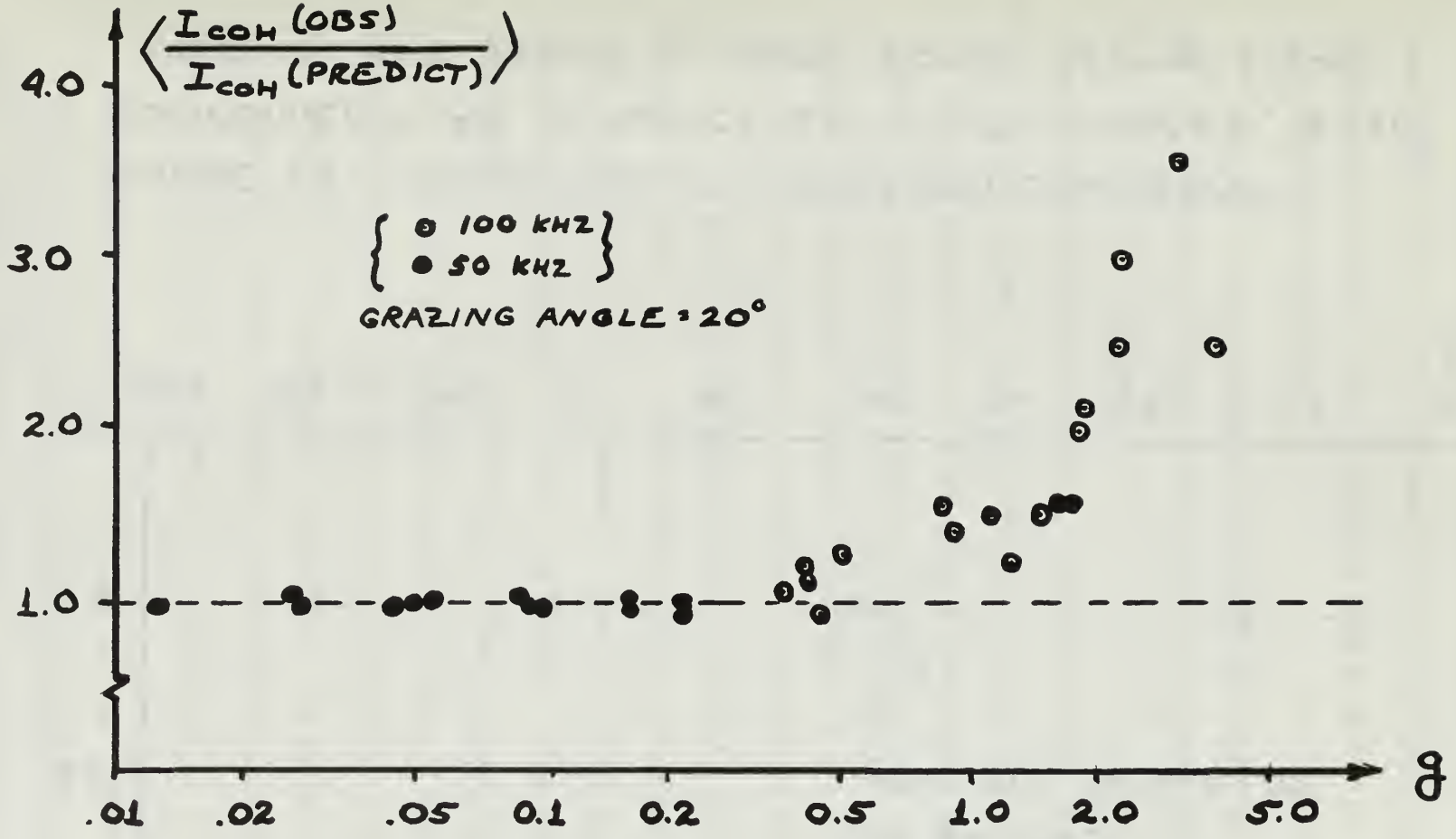

FIGURE 28 - DEPARTURE OF OBSERVED COHERENT COMPONENT FROM THEORY AS A FUNCTION OF ROUGHNESS AT $\theta = 20°$.

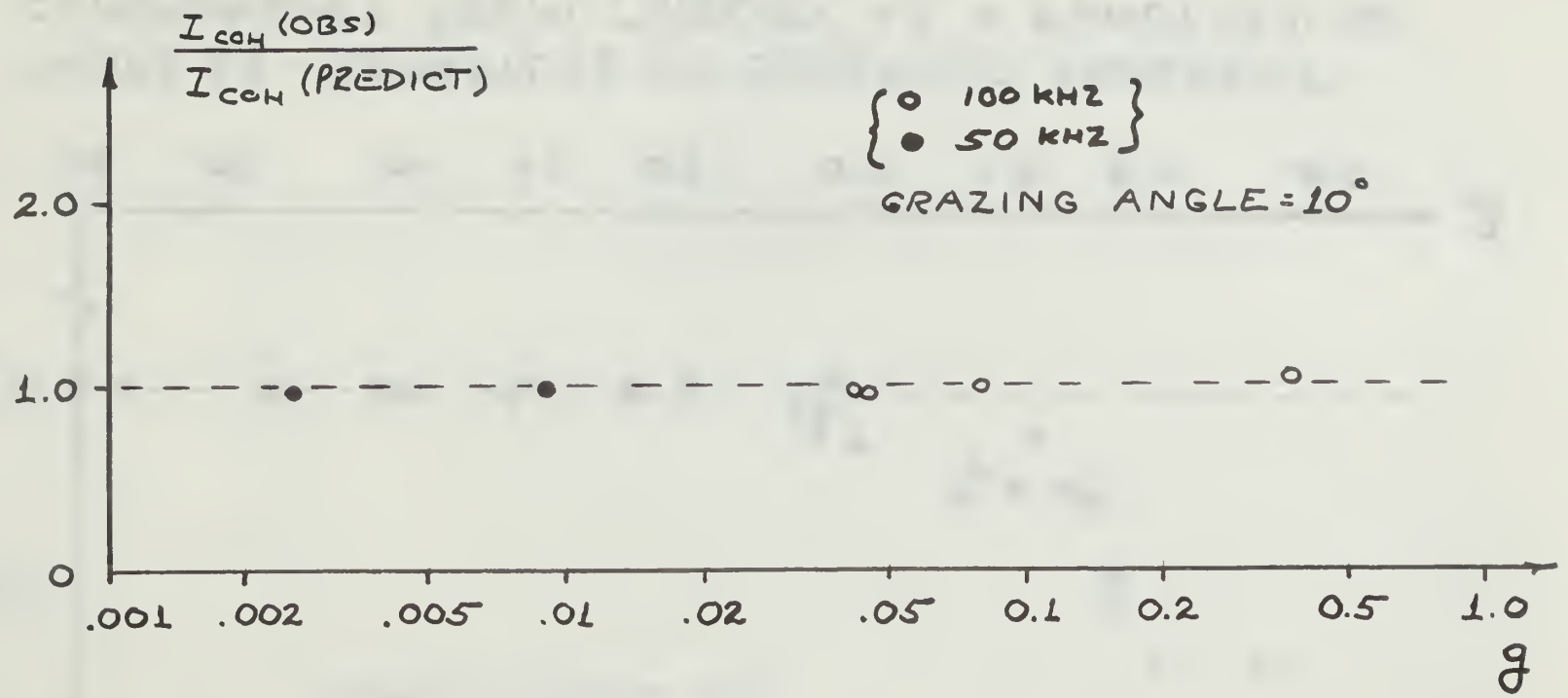

FIGURE 29 - BEHAVIOR OF OBSERVED COHERENT COMPONENT AS A FUNCTION OF ROUGHNESS, $\theta = 10°$
(VERTICAL AXIS DRAWN TO SAME SCALE AS FIGS 27, 28)

all points were well above the predicted value of unity, and well beyond experimental error. This phenomenon was again manifest during the study of scatter for sound beam cross versus beam parallel to sea propagation direction (see figure 31).

Since this gross departure from theory was noted only in the vicinity of $\theta = 20°$ with the roughest wind-driven sea, these parameters were held constant, and the frequency was varied from 50 to 130 kHz in ten kHz steps. The resulting data points, plotted in figure 26, show the onset of the excess coherent component at just above 50 kHz.

All data points for 20° grazing angle are plotted against surface roughness, g, in figure 28. Here, $\left\langle \frac{I_{coh}(obs)}{I_{coh}(predict)} \right\rangle$ appears to be a monotonically increasing function in the range $0 < g < 3.0$. The phenomenon cannot be attributed to increasing roughness alone, however, since at $\theta = 30°$ even higher roughnesses were attained without this behavior, as shown in figure 27. Similar data, taken at 10° grazing angle, are shown in figure 29; the phenomenon in question does not appear, but it should be noted that for all points $g < 0.4$. Investigation of larger roughnesses at 10° grazing will require sound frequencies in the range 130 kHz < f < 250 kHz, a region in which the EDO-327 transducers were not designed to operate. (250 kHz is the high frequency limit on inputs to the PAR-101 Correlation Function Computer). The study of this departure from theory is therefore incomplete, and investigation of larger roughnesses (through higher frequencies) is necessary.

B. COMPARISON OF CROSS-SEA WITH PARALLEL-SEA SCATTERING

The width of the anechoic tank limited transducer separation to 52" (132 cm) for cross sea scatter (figure 4). If the distance from transducer face to the beginning of the far field is taken to be $x = 2a^2/\lambda$,

where a = piston radius = 11 cm, then $x = 81$ cm and 162 cm for 50 kHz and 100 kHz, respectively. Since the 52" spearation clearly placed the ensonified surface in the near field, for comparison it was considered necessary to maintain this same geometry for parallel sea scatter (although much more space was available).

The curves of figures 30 through 33, which compare cross and parallel scatter, differ in detail from the corresponding data taken at 18' transducer spacing, possibly due to operation in the near field. For this reason, the data obtained at 52" separation were not used to study dependence of specular, coherent scattering on roughness, but were only used to infer information concerning cross versus parallel scattering.

Figures 30 through 33 show $\left\langle \frac{I_{coh}(obs)}{I_{coh}(predict)} \right\rangle$ versus grazing angle for both cross and parallel scatter. In almost every case, it is seen that cross scatter gave a somewhat stronger specular coherent return than was observed for the corresponding parallel case. The noticeable drop which occurred at 100 kHz, 30° grazing angle was outside the bounds of experimental uncertainty; since it was not present at the greater transducer separation, it appears to be attributable to either near field operation or to the reduction in ensonified area (by a factor of about 6).

It should be noted that the larger than expected coherent component at $\theta = 20°$, sea "C" occurs in figure 31, for both cross and parallel scattering.

C. SURFACE SHADOWING

The shadowing function, $S(\theta)$, derived by Wagner [Ref. 5] and defined in section II-B uses ray acoustics, neglecting diffraction as well as multiple reflections. The ray approximation should improve with increasing σ/λ, becoming precise in the limit as $\sigma/\lambda \to \infty$. Wagner states that the

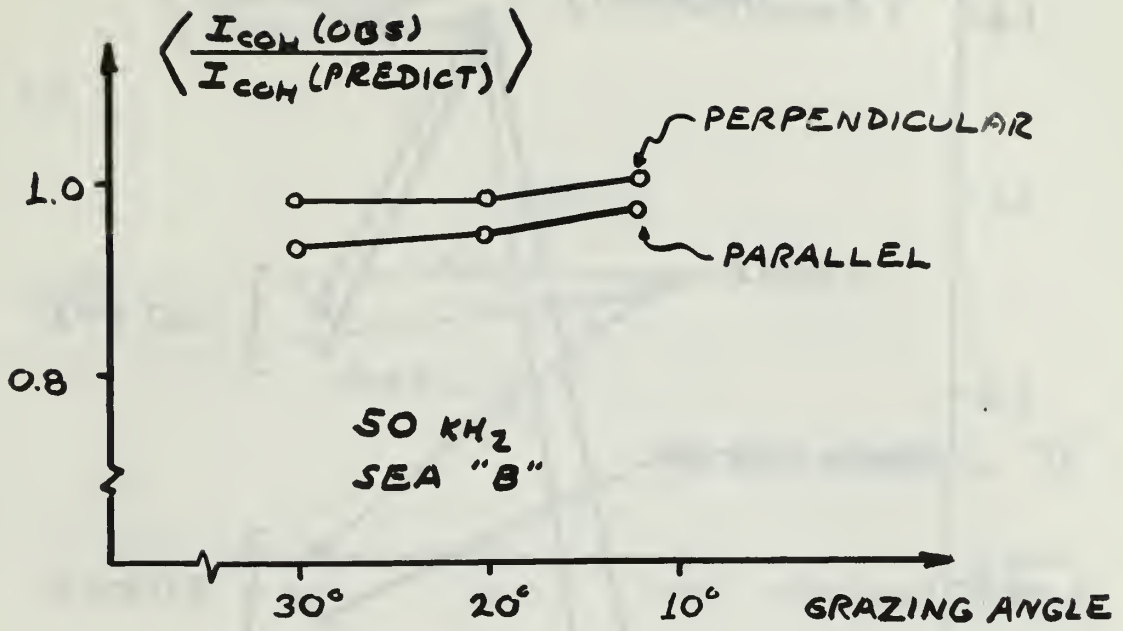

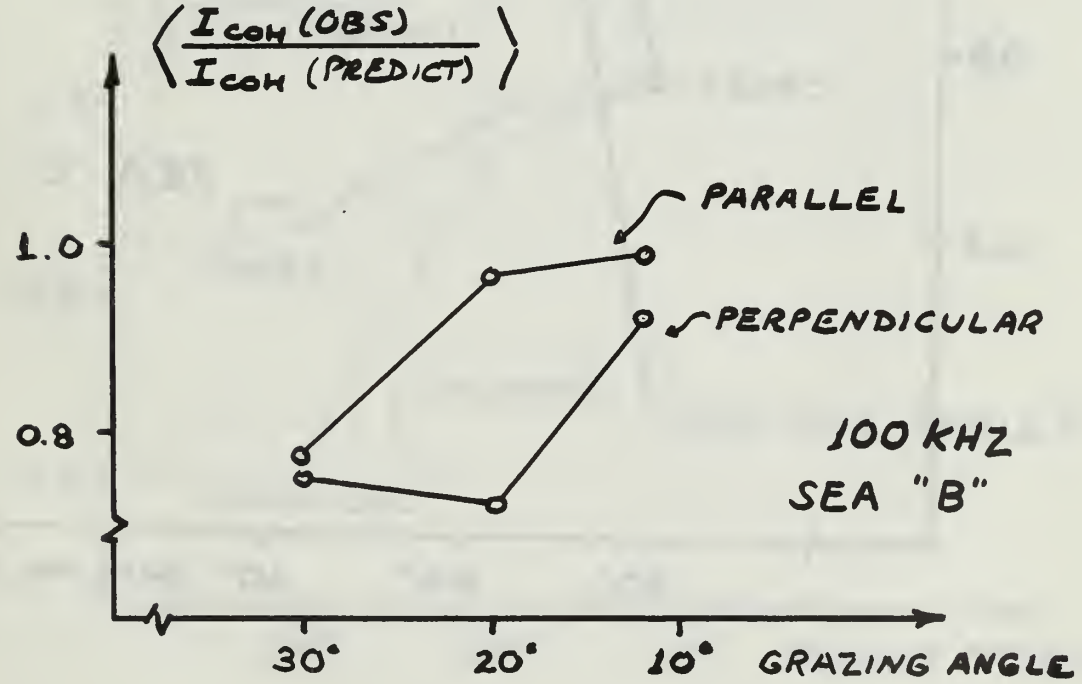

FIGURE 30 - PARALLEL AND CROSS SCATTERING COMPARED FOR SEA "B"

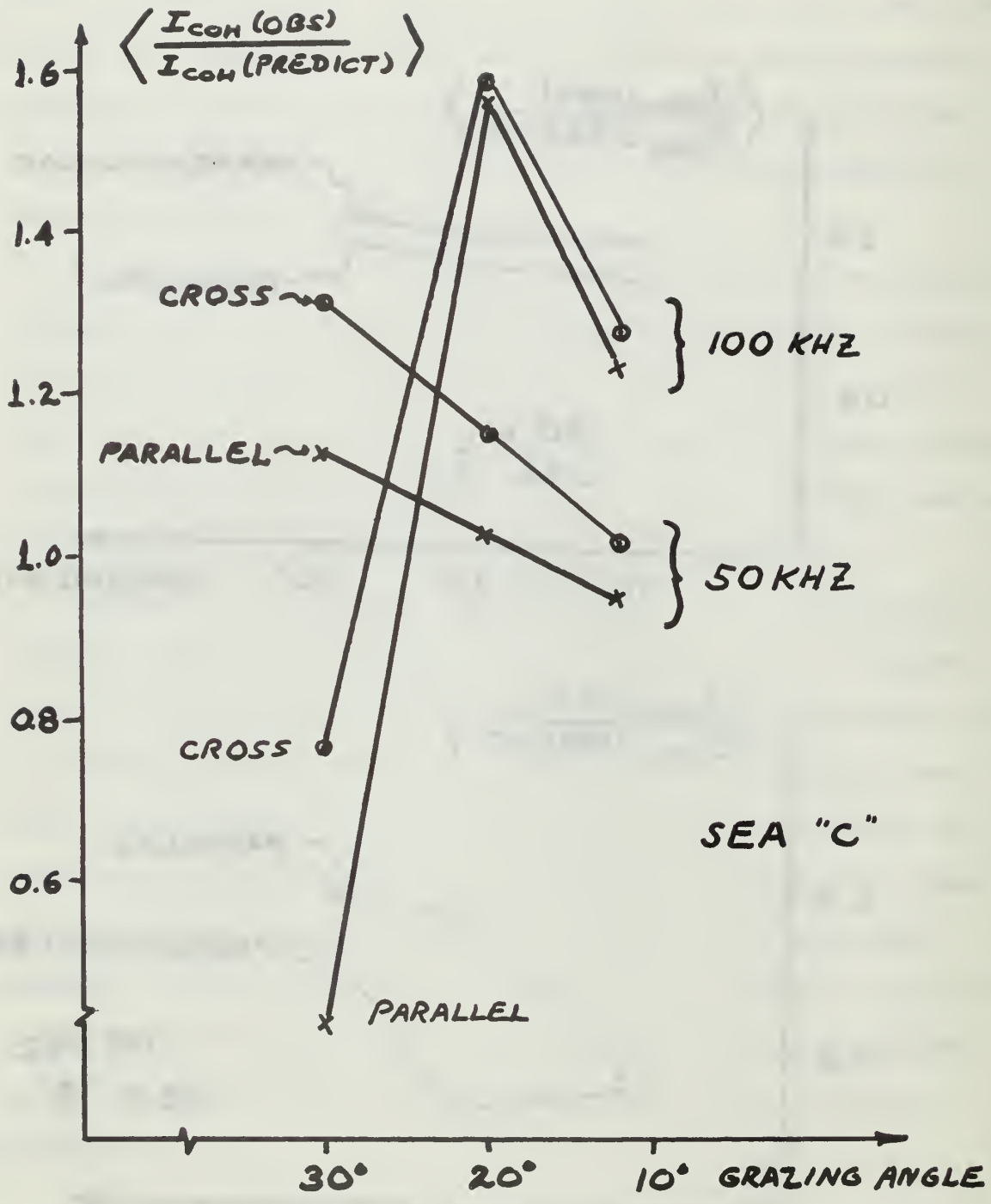

FIGURE 31 - PARALLEL AND CROSS SCATTERING COMPARED FOR SEA "C"

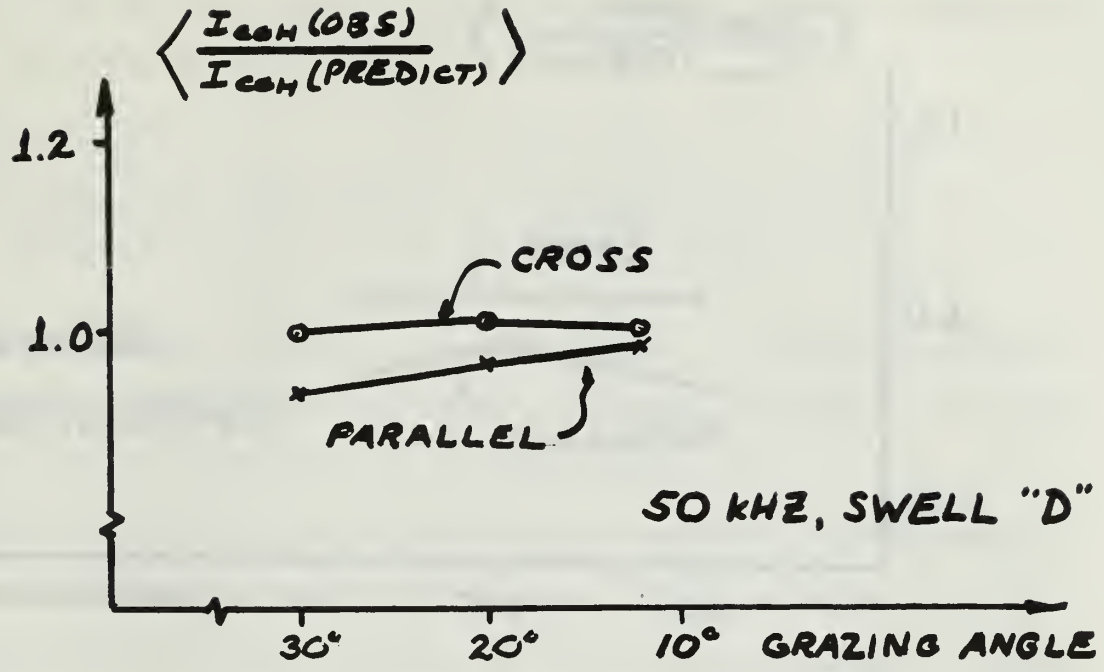

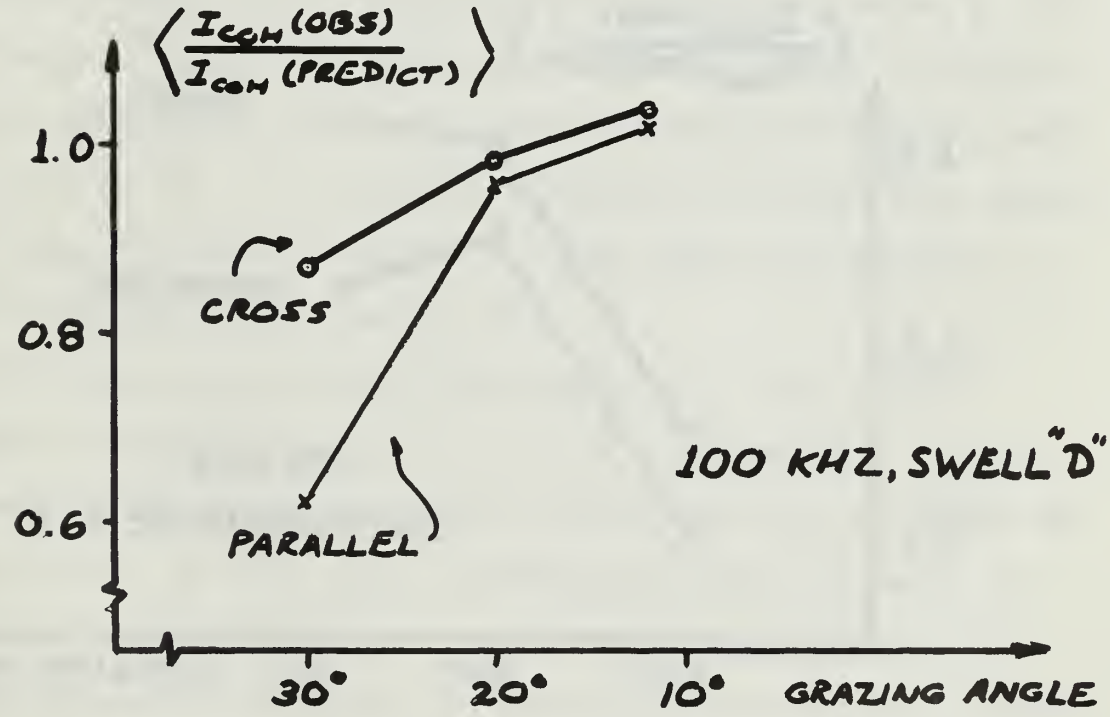

FIGURE 32 - PARALLEL AND CROSS SCATTERING COMPARED FOR SWELL "D"

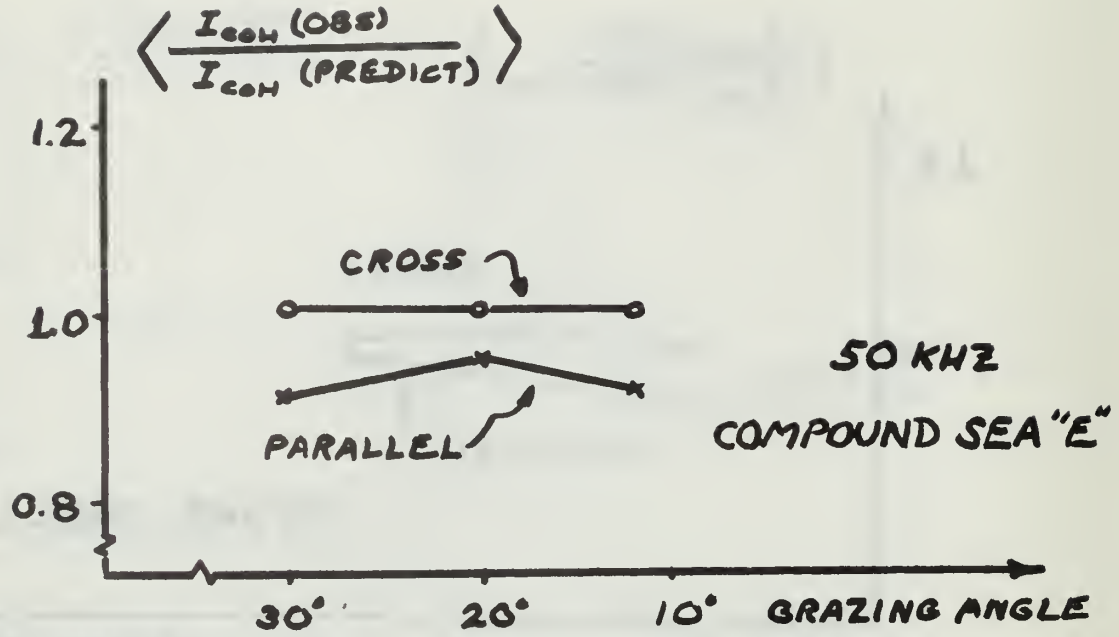

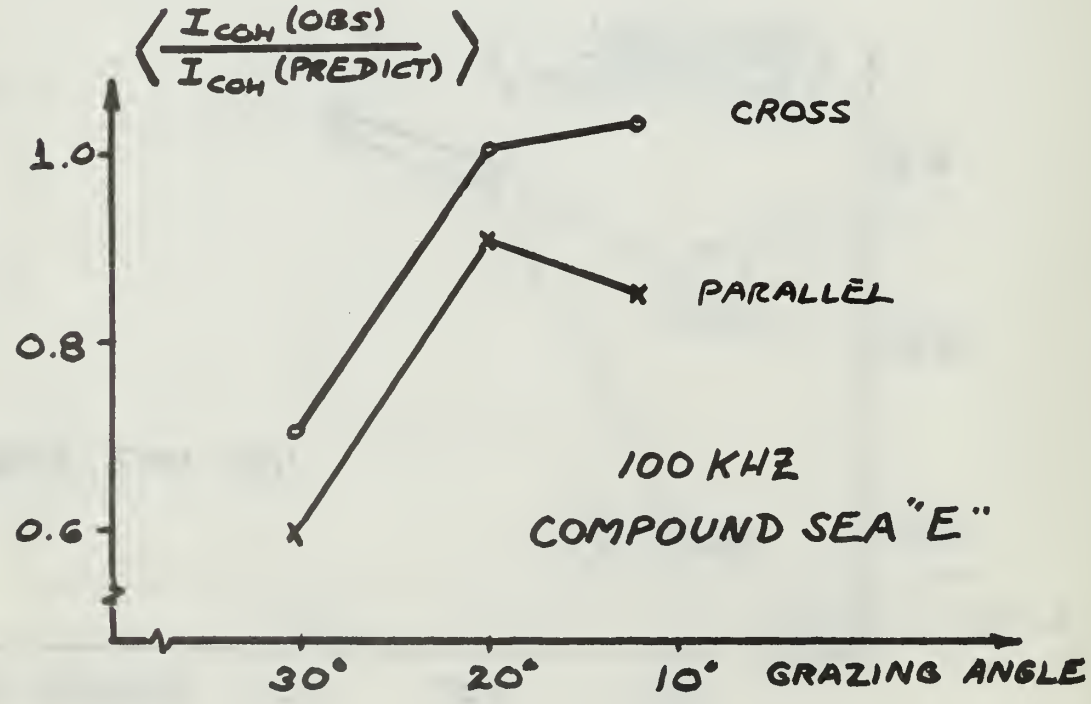

FIGURE 33 - PARALLEL AND CROSS SCATTERING COMPARED FOR COMPOUND SEA "E"

correct use of the shadowing function for specular, coherent intensity is multiplication by $S^2(\theta)$. Thus

$$\left\langle \frac{I_{coh}}{I_{mirror}} \right\rangle = S^2(\theta)\, e^{-g} \quad , \text{ or } \left\langle \frac{I_{coh}(obs)}{I_{coh}(predict)} \right\rangle = S^2(\theta)$$

The arguments of $S(\theta)$ are θ, σ, and L where L = surface correlation distance in the scattering direction. The sound wavelength, λ, does not appear, but use of the ray theory implies that $\sigma >> \lambda$.

The spatial surface correlation function measured in the scattering direction (up-down wind) resembles a damped cosine curve [Ref. 7]. If the correlation distance (distance for the correlation function to reach 1/e of its initial value) is determined using the decay envelope, L 14.0 cm; however, if L is computed from the cosine-like function in its first quarter period (prior to the first crossing of the zero correlation axis) L 3.0 cm results. The correlation distances are indicated to be approximate, since they were obtained for a slightly smaller sea generated by a set of fans which is no longer installed.

The transducers used limited the value of σ/λ to 0.3 and less. Although this obviously does not satisfy the requirement that $\sigma >> \lambda$, data obtained were compared to Wagner's predictions (Fig. 34) plotted for convenience at $\sigma/\lambda = 10$. Lack of experimental data in the region 0.5 $0.5 << \sigma/\lambda < 10.0$ precludes extrapolation and leaves unanswered the question whether the correlation distance computed from the decay envelope (L = 14.0 cm) more accurately predicts the degree of shadowing than does L = 3.0 cm

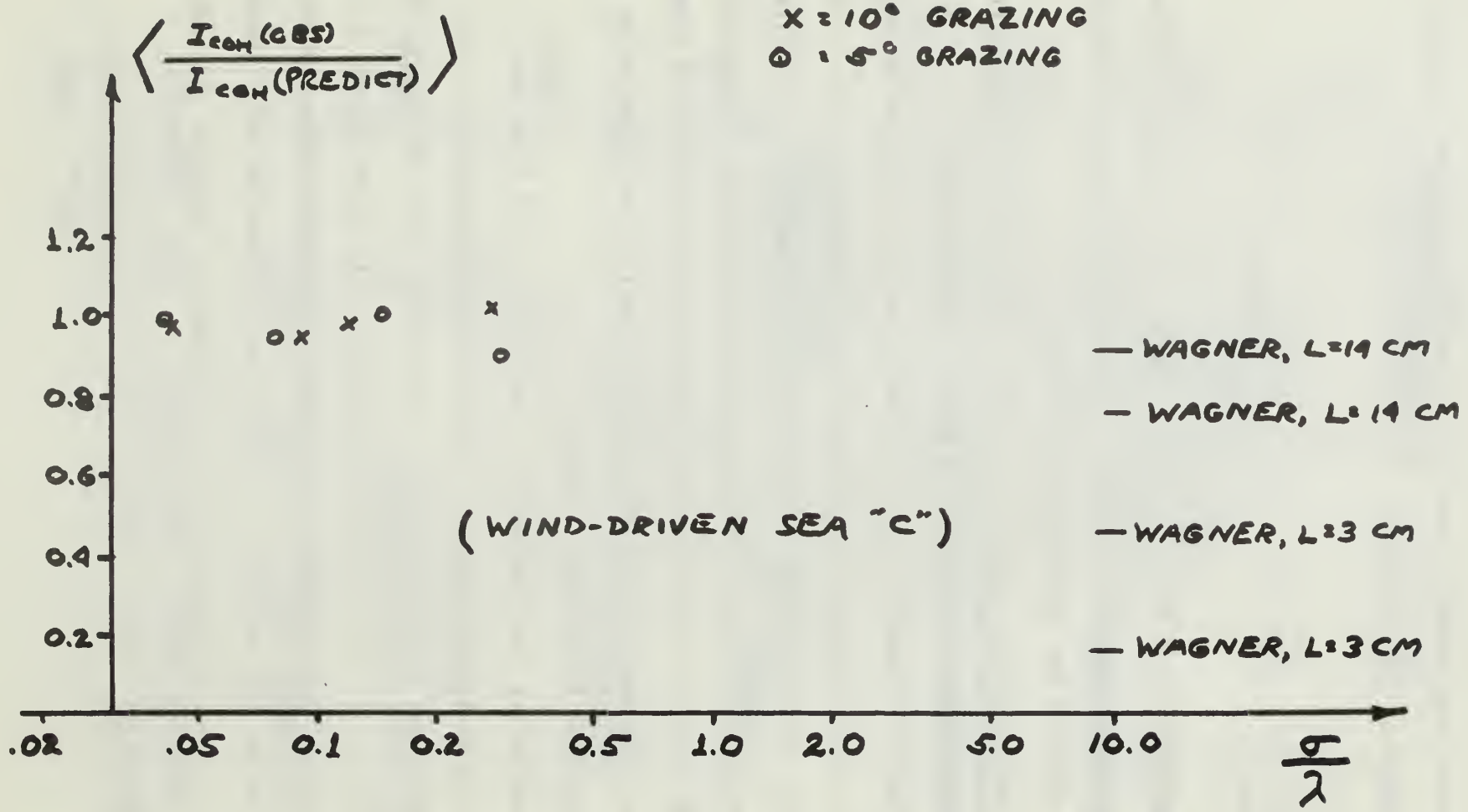

FIGURE 34 - OBSERVED SHADOWING AS A FUNCTION OF σ/λ
(RAY APPROXIMATION CONSIDERED VALID FOR $\sigma/\lambda \geq 10.0$

V. CONCLUSIONS

The unpredicted growth of the coherent component of scattered intensity in figures 23, 26, and 28 may be the same phenomenon described by Medwin [Ref. 1]. While conducting normal-incidence, specular scattering from a wind driven surface, Medwin observed that above a critical frequency "the instantaneous scattered intensity is a nonstationary, oscillating function of frequency, varying about the asymptotic value." He postulated that this oscillation with frequency was due to alternate destructive and constructive interference of incident and reflected sound waves from statistically prominent facets of the surface, whose distribution of wave heights was Gaussian. Medwin suggested that the dimension causing the interference was perhaps the distance between mean positive and mean negative wave heights, and noted that the phenomenon was absent for $\sigma << \lambda$. He defined the critical frequency as that for which $\lambda/4$ = facet separation (the first interference with increasing frequency).

Non-normal sound beam incidence and surface anisotropy greatly complicate definition of the facets responsible for interference. Examination of figures 30 through 33 (particularly the 100 kHz curves of Fig. 31) indicates little, if any dependence of the behavior on surface anisotropy; thus, if this is an interference phenomenon, it suggests that the governing parameters are functions of λ, σ, and θ, and are not influenced by correlation distance.

Comparison of parallel-sea with cross-sea scattering shows that the cross-sea geometry gives a coherent component which is in general consistently larger than that obtained for the corresponding parallel-sea case (Figs. 30 through 33). This difference in coherent component may have

been due to the different off-specular rays for the two cases; these rays, which are excluded in theoretical solutions, are inevitably collected during an experiment in spite of the use of directional transducers.

Specular, coherent scattering from pure swell (whose wave height probability density is strongly non-Gaussian) appears to closely obey the e^{-g} prediction, although this function was derived for a Gaussian distribution of surface wave heights. The high-frequency limit of the EDO-327 transducers and the relatively small RMS swell wave height ($\sigma \leq 0.15$ cm) restricted the attainable values of g to $0 < g \leq 0.1$. For completeness, behavior of specular, coherent scattering in the range $0.1 \leq g \leq 5.0$ should be studied.

The energy spectral density for sea-swell combination "E" [Fig. 15] shows that about 20% of total energy is carried by the swell. The corresponding wave height probability density function, however, appears as near to Gaussian as any of the purely wind-driven seas (Fig. B-5). Nonlinear wave interaction caused the energy spectrum of the sea-swell combination to be significantly different from that produced by superposition of its two constituent spectra (see Figs. 13, 14, and 15).

Wagner's Shadowing Correction (Sec. II-B), based on ray acoustics, tended to overcorrect, due no doubt to the partial illumination of "shadowed" areas caused by wave diffraction. In figure 34 it is not possible to extrapolate to a higher value of σ/λ, where the ray theory should be more valid, in order to determine whether the proper correlation distance to use in the computation of Wagner's correction should be derived from the envelope of the spatial correlation function.

At the time of this experimental work, transducers were being fabricated to cover the frequency range $120 \leq f \leq 240$ kHz. Investigation of specular scattering in this frequency range is necessary to clarify many of the phenomena observed.

APPENDIX A — ANALYSIS OF ERROR

Several important calculated quantities concerning scattered sound depend on oscilloscope readings and the wave staff calibration. It was possible to estimate the degrees of uncertainty in these constituent quantities, and their effect on the relative coherent intensity and incoherent intensity compared with theory is now considered. The method used is the finite differential approximation to the derivative.

1. Uncertainty in $\left\langle \frac{I_{coh}(obs)}{I_{coh}(predict)} \right\rangle$

This ratio, which compares the observed to predicted specularly scattered coherent intensity, is called I for brevity in the analysis.

$$I \equiv \left\langle \frac{I_{coh}(obs)}{I_{coh}(predict)} \right\rangle = \frac{A^2}{e^{-g}} = A^2 e^{g}$$

$$= \frac{N^2}{M^2} \, e^{k^2\sigma^2(2 \sin \theta)^2}$$

where: N = maximum value of rough surface cross-correlation, read from scope

M = maximum value of mirror surface cross-correlation, read from scope.

It is assumed that k and θ are known exactly; sources of uncertainty are M, N, and σ.

Let:

$\frac{\delta I_N}{I}$ = relative uncertainty in I due to N

$\frac{\delta I_M}{I}$ = relative uncertainty in I due to M

$$\frac{\delta I_\sigma}{I} = \text{relative uncertainty in I due to } \sigma$$

The total relative error is the sum of the contributions:

$$\frac{\delta I_{total}}{I} = \frac{\delta I_N + \delta I_M + \delta I_\sigma}{I}$$

By partial differentiation:

$$(1) \quad \frac{\partial I}{\partial N} = \frac{2N}{M^2} e^g = \frac{2I}{N}$$

$$(2) \quad \frac{\partial I}{\partial M} = \frac{-2N^2}{M^3} e^g = \frac{-2I}{M}$$

$$(3) \quad \frac{\partial I}{\partial \sigma} = A^2\, 2k^2\, \sigma\, (2 \sin\theta)^2\, e^g = \frac{2gI}{\sigma}$$

Using the finite differential approximation and rearranging, equations (1), (2), and (3) become:

$$(4) \quad \frac{\delta I_N}{I} = 2\,\frac{\delta N}{N}$$

$$(5) \quad \frac{I_M}{I} = -2\,\frac{\delta M}{M}$$

$$(6) \quad \frac{I_\sigma}{I} = 2g\,\frac{\delta\sigma}{\sigma}$$

$$\frac{\delta I_{total}}{I} = 2\,\frac{\delta N}{N} - \frac{\delta M}{M} + g\,\frac{\delta\sigma}{\sigma}$$

where $\frac{\delta N}{N}$, $\frac{\delta M}{M}$, and $\frac{\delta\sigma}{\sigma}$ are the constituent relative uncertainties. It can be seen taht the "worst case" will occur when the following three conditions are simultaneously satisfied:

a. N is small

b. g is large

c. δM is negative, while δN and $\delta\sigma$ are positive.

It should be noted that the value of M is controllable; its magnitude is set for almost full oscilloscope deflection at the start of each data run by adjusting the correlator input gains.

For the "worst case" analysis, typical parameters from a large roughness data run were used. In all cases, the oscilloscope readings were judged accurate to ±.1 cm.

$$g = 3.0$$

$$\frac{\delta N}{N} = \frac{.1 \text{ cm}}{2. \text{ cm}} = .050$$

$$\frac{\delta M}{M} = \frac{-.1 \text{ cm}}{9.0 \text{ cm}} = -.011$$

$$g\left(\frac{\delta\sigma}{\sigma}\right) = 3.0\left(\frac{.01 \text{ cm}}{.40 \text{ cm}}\right) = .075$$

$$\frac{\delta I_{total}}{I} = 2(.050 + .011 + .075) = .272 = \underline{\underline{27.2\%}}$$

2. Uncertainty in $\left\langle \frac{I(\text{incoherent})}{I(\text{mirror})} \right\rangle$

If the method of section III-C-2 had been used to isolate the incoherent intensity, uncertainties of unacceptable magnitude would have resulted, as will no be shown. Define:

$$H \equiv \left\langle \frac{I(\text{incoh})}{I(\text{mirror})} \right\rangle = R - A^2 \qquad \text{(from section III-C-2)}$$

$$= \frac{D}{C} - \frac{N^2}{M^2}$$

where: D = maximum value of rough surface autocorrelation, read from oscilloscope

C = maximum value of mirror surface autocorrelation, read from oscilloscope

By the method of finite differentials

$$\frac{H_{total}}{H} = \frac{R\left[\frac{\delta D}{D} - \frac{\delta C}{C}\right] + 2A^2\left[\frac{\delta M}{M} - \frac{\delta N}{N}\right]}{R - A^2}$$

Using parameters which occurred during an actual data run, (Run 25-E-100):

$g = .36$

$R = .713$

$A^2 = .671$

$$\frac{\delta C}{C} = \frac{\delta M}{M} = -\frac{.1 \text{ cm}}{10. \text{ cm}} = -.01 \quad \text{(negative for worst case)}$$

$$\frac{\delta D}{D} = \frac{\delta N}{N} = \frac{.1 \text{ cm}}{5. \text{ cm}} = .02$$

$$\frac{\delta H}{H} = \frac{(.713)(.03) + 2(.671)(.03)}{.042} = 1.45 = \underline{145\%}$$

The difficulty arises in the term $(R - A^2)$; the two numbers are nearly equal, and each has significant relative error. The above calculation gives a conservative estimate of the uncertainty, since it does not consider the non-simultaneity of cross and autocorrelations in the presence of statistical temporal variations. In order to obtain the incoherent intensity, it would have had to be calculated or measured directly, rather than computed by subtraction.

APPENDIX B — PROBABILITY DENSITY FUNCTIONS OF THE SURFACE WAVE HEIGHTS

The probability density of wave heights was determined for each of the representative scattering surfaces as follows:

1. With the wave staff located at the center of the scattering area, a ten minute tape recording was made of the wave record, $z(t)$.

2. The wave record was replayed at ten times speed into the analog-to- digital converter of the CI5000/SDS9300 hy brid computer. The converter sampled the analog signal, $z(10t^*)$, at a rate of 333 Hz, until an ensemble of 10^4 digital wave heights was generated. (t^* is time in the playback-digitize frame).

3. The mean and standard deviation of the ensemble were computed; the ensemble mean was then adjusted to zero by subtracting the previously calculated mean from each ensemble member.

4. The SDS9300 digital computer then sorted the ensemble values into' intervals of width $c\sigma$, where σ = ensemble standard deviation, and c was a constant to be optimized.

5. Total "area" under the resulting probability density histogram was 10^4 (the number of observations). Dividing each ordinate value by 10^4 then gave a probability density whose area was normalized to unity.

The appearance (and utility) of the density functions obtained was dependent upon the interval width selected; larger widths produced a smooth plot, but tended to suppress all but the gross features, while too narrow an interval gave an irregular plot due to sparsity of interval population. Figure B-2, made with an interval width = 0.05σ , illustrates the latter phenomenon.

For all wave-height probability densities (except pure swell), a standard Gaussian curve normalized in units of σ was plotted for comparison. These analytical curves are represented by solid lines, while the observed density function is given by points.

The wave-height probability density of pure swell (Fig. B-4) resembles that of a sine wave, even though its frequency-domain structure (Fig. 14) is by no means a delta function.

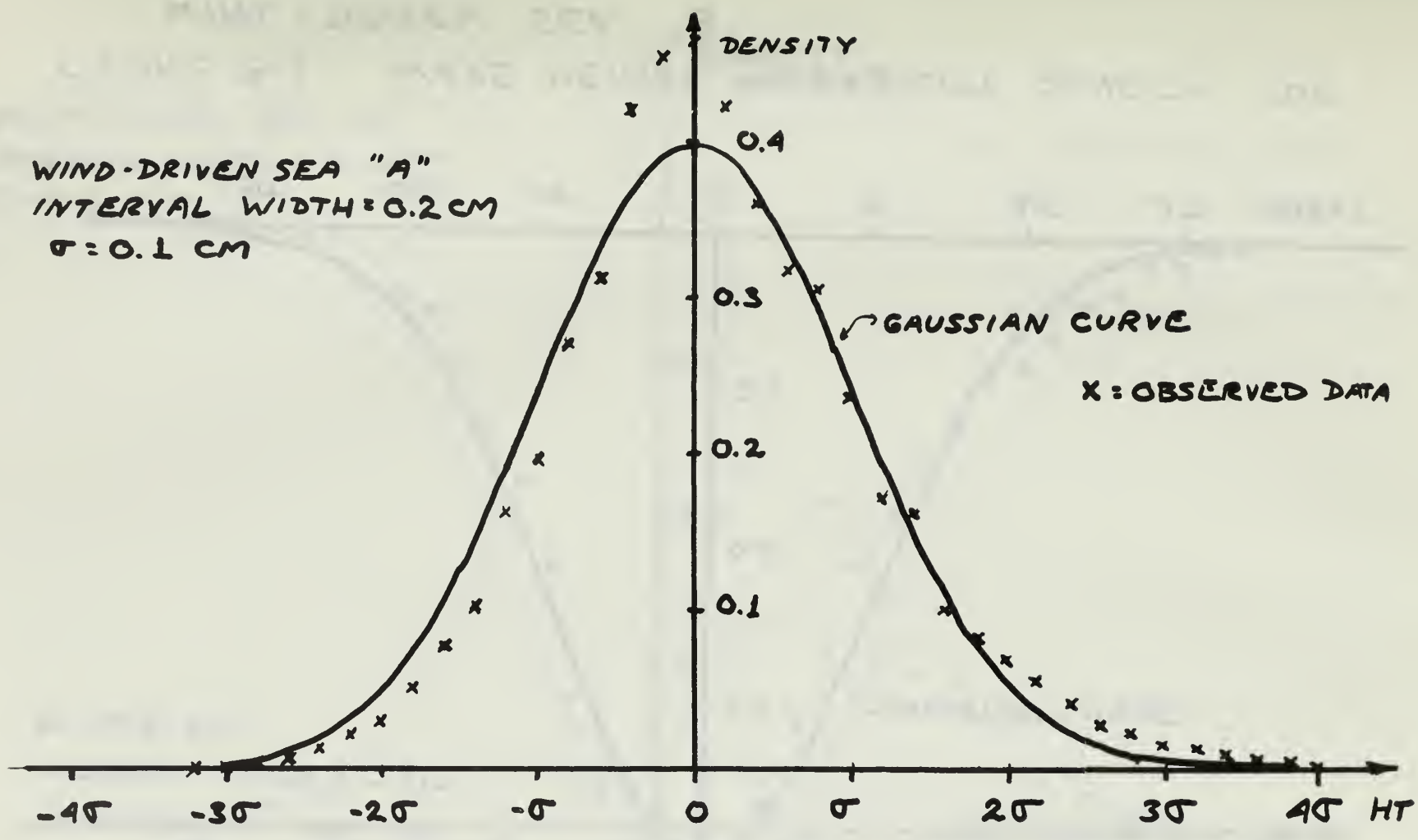

FIGURE B-0 WAVE HEIGHT PROBABILITY DENSITY FOR WIND-DRIVEN SURFACE "A"

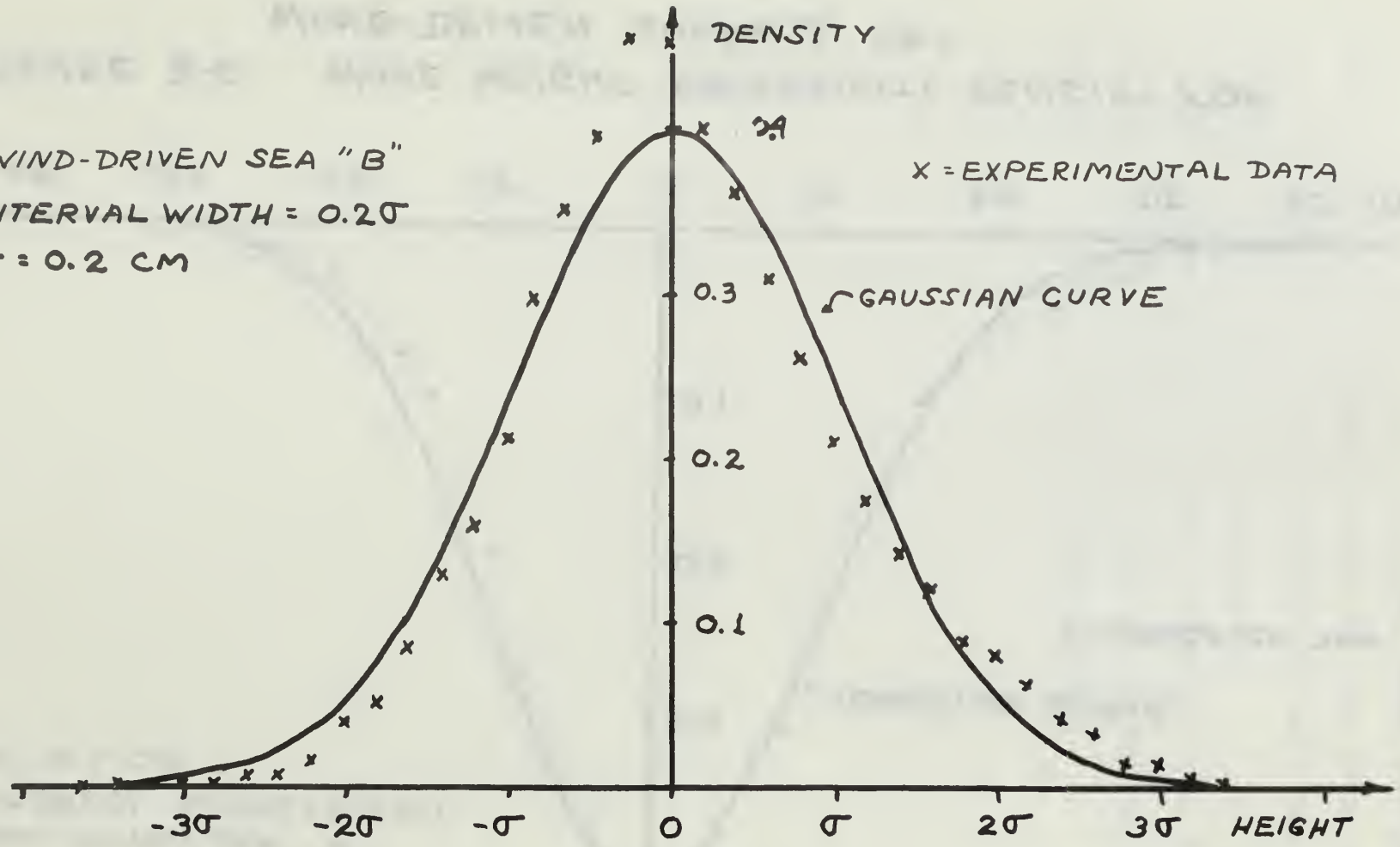

FIGURE B-1 WAVE HEIGHT PROBABILITY DENSITY FOR WIND-DRIVEN SEA "B"

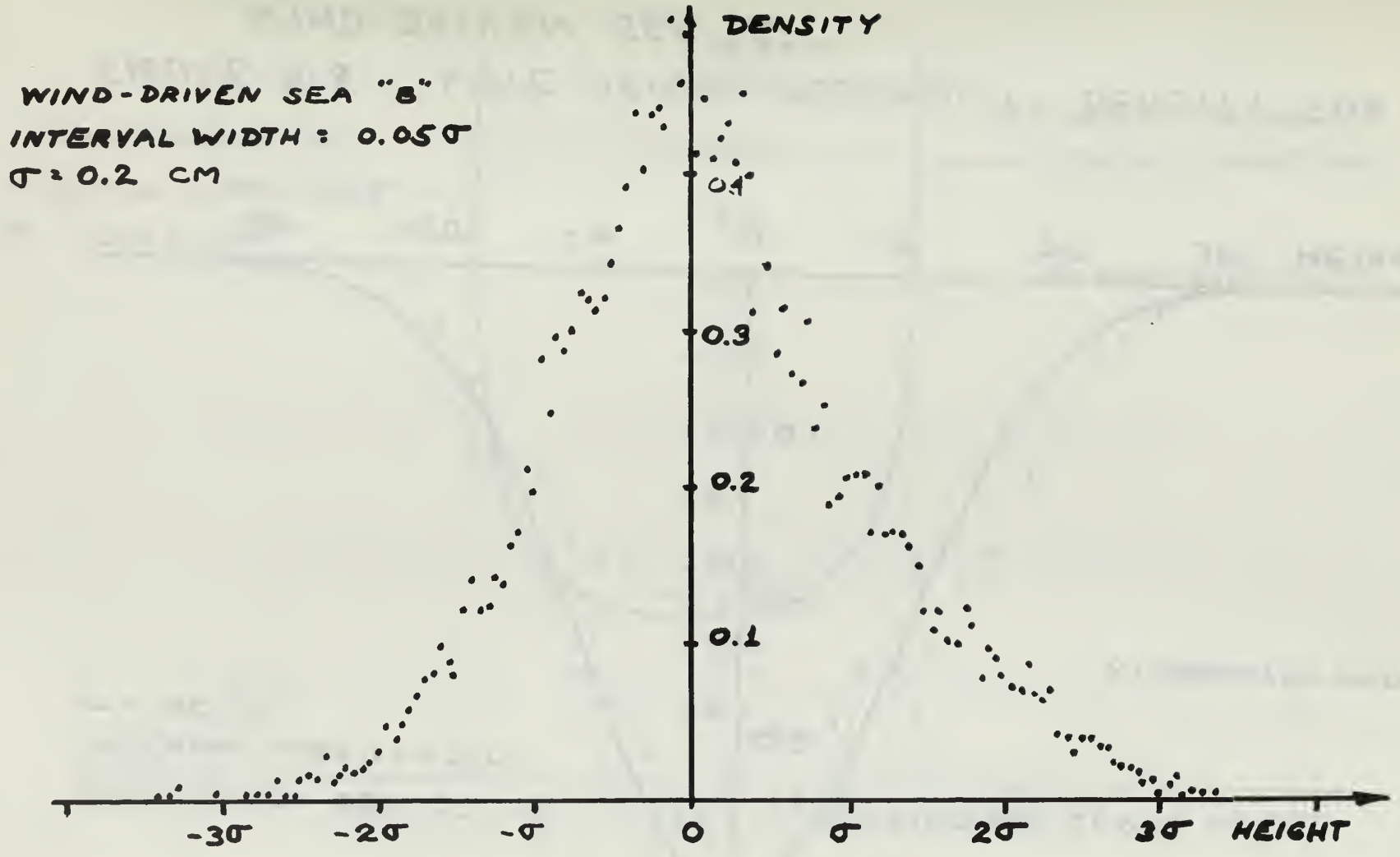

FIGURE B-2 - IRREGULARITY CAUSED BY SELECTION OF TOO-NARROW INTERVALS. (COMPARE WITH FIG B-1)

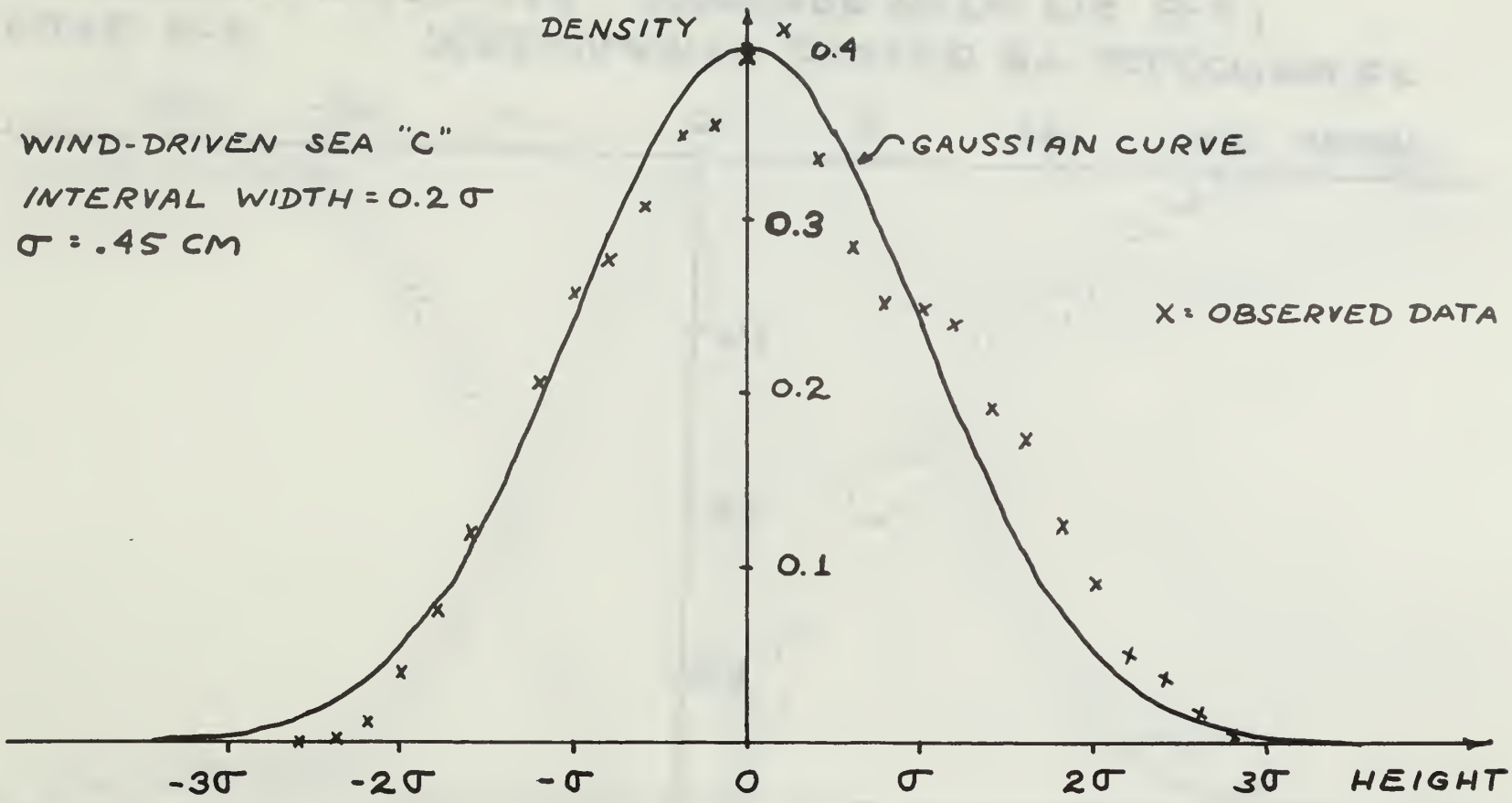

FIGURE B-3 WAVE HEIGHT PROBABILITY DENSITY FOR WIND-DRIVEN SEA "C"

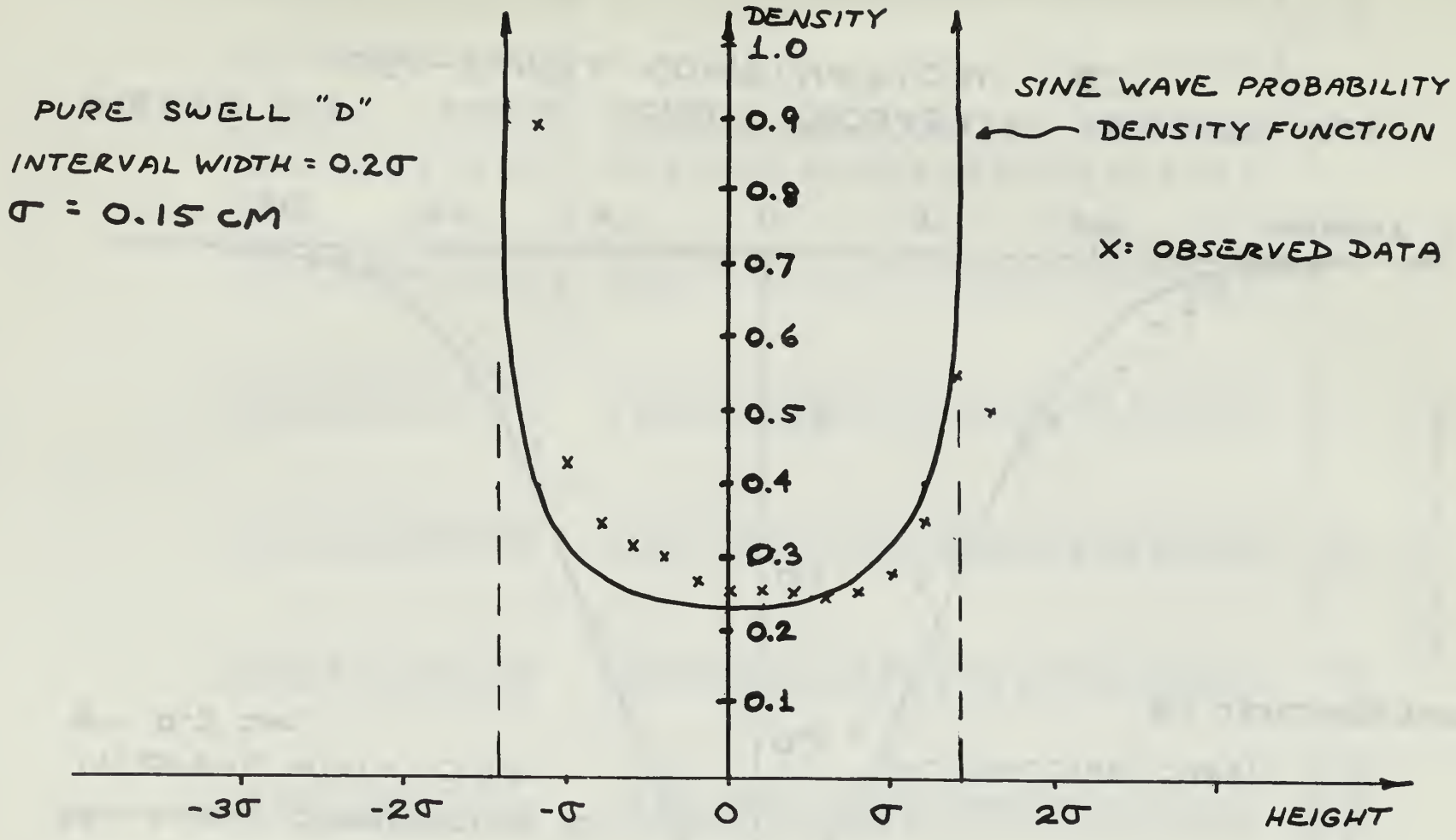

FIGURE B-4 WAVE HEIGHT PROBABILITY DENSITY FOR PURE SWELL "D"

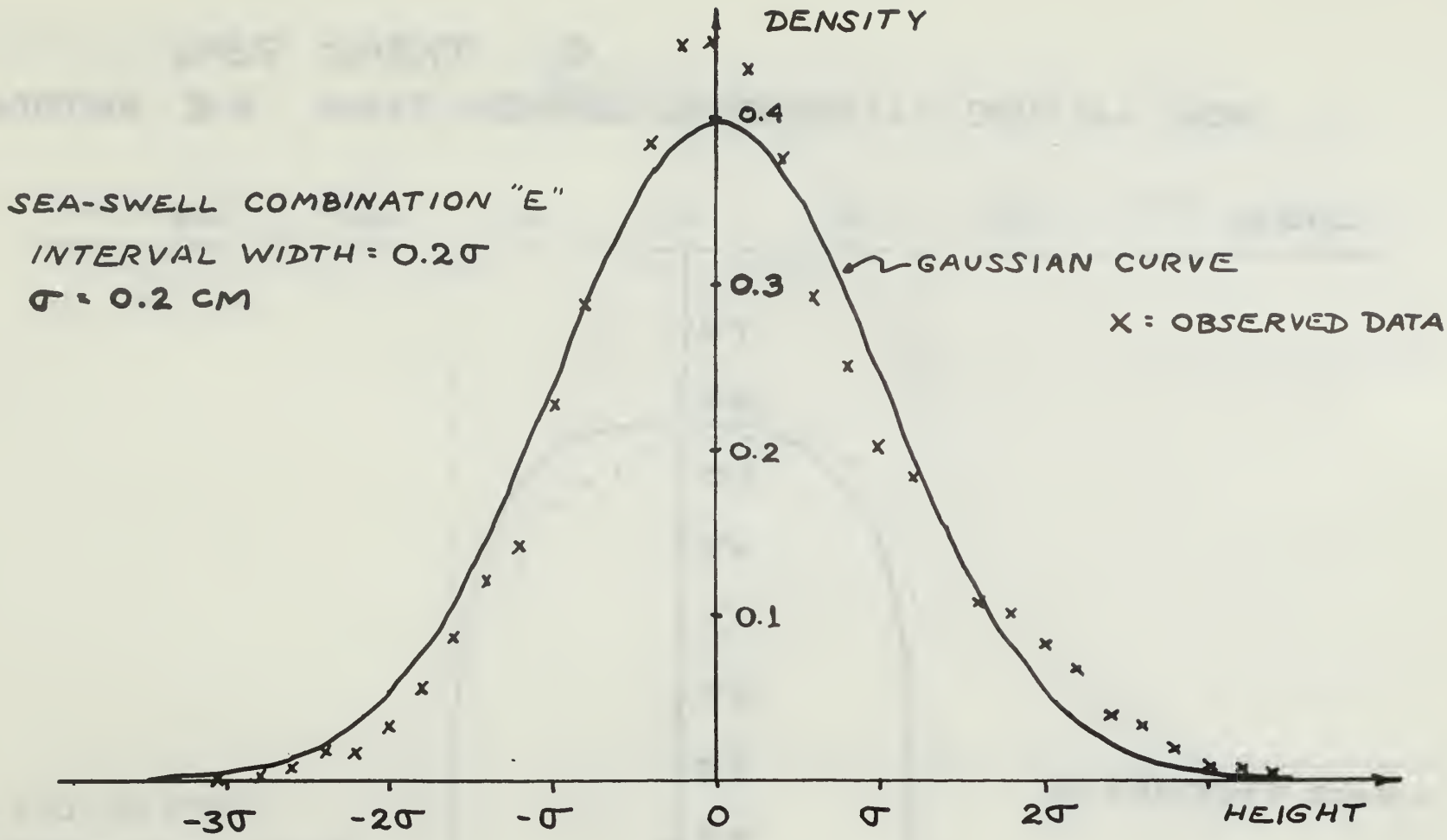

FIGURE B-5 WAVE HEIGHT PROBABILITY DENSITY FOR SEA-SWELL COMBINATION "E"

APPENDIX C — SUMMARY TABLES OF DATA

Freq.	θ	λ	σ	λ/σ	g	e^{-g}	$\frac{I_{total}}{I_{mirror}}$	$\frac{I_{coh}(obs)}{e^{-g}}$
LONG SEPARATION:								
50	30	2.96	.15	.051	.101	.904	.880	.97
50	25	2.96	.15	.051	.072	.930	.897	.96
50	20	2.96	.155	.052	.051	.950	.920	.98
50	15	2.96	.14	.047	.024	.976	.973	.98
50	10	2.96	.128	.043	.009	.997	.975	.99
50	5	2.96	.120	.041	.002	1.000	.996	.99
50	30	2.96	.42	.142	.794	.451	.541	1.18
50	20	2.96	.455	.154	.436	.647	.706	1.08
50	15	2.96	.435	.147	.229	.795	.830	1.01
50	10	2.96	.389	.131	.083	.920	.892	.99
50	5	2.96	.427	.144	.025	.975	.985	1.01
50	30	2.96	.07	.024	.022	.978	.987	.99
50	25	2.96	.063	.021	.013	.987	.993	1.00
50	20	2.96	.05	.017	.005	.995	1.000	.99
50	15	2.96	.031	.010	.001	.999	.996	.99
50	10	2.96	.042	.014	.001	1.000	1.000	1.00
50	5	2.96	.035	.012	$\sim$0	1.000	1.000	1.00
50	30	2.96	.155	.052	.108	.904	.874	.97
50	25	2.96	.167	.056	.090	.914	.891	.97
50	20	2.96	.15	.051	.047	.954	.938	.96
50	15	2.96	.15	.051	.027	.973	.959	.98
50	10	2.96	.126	.043	.009	.992	.981	.99
50	5	2.96	.145	.049	.003	1.000	.990	.99
50	25	2.96	.403	.136	.525	.591	.610	1.00
SHORT SEPARATION (With Wind):								
50	12	2.96	.134	.045	.014	.986	.940	.97
50	12	2.96	.455	.154	.161	.852	.818	.95
50	12	2.96	.150	.051	.017	.983	.979	.99
50	12	2.96	.217	.073	.037	.963	.906	.94
50	30	2.96	.141	.048	.089	.914	.857	.94
50	30	2.96	.429	.145	.825	.438	.543	1.13
50	30	2.96	.086	.029	.033	.967	.935	.94
50	30	2.96	.194	.066	.169	.844	.779	.92
50	20	2.96	.146	.049	.045	.956	.917	.95
50	20	2.96	.422	.142	.375	.687	.747	1.03
50	20	2.96	.116	.039	.028	.972	.959	.98
50	20	2.96	.216	.073	.098	.907	.870	.96

Freq.	θ	λ	σ	λ/σ	g	e^{-g}	$\frac{I_{total}}{I_{mirror}}$	$\frac{I_{coh}(Obs)}{e^{-g}}$
SHORT SEPARATION (Cross-wind):								
50	30	2.96	.153	.052	.105	.900	.902	.986
50	30	2.96	.467	.158	.980	.375	.554	1.310
50	30	2.96	.120	.041	.065	.937	.972	1.000
50	30	2.96	.225	.076	.228	.796	.879	1.013
50	12	2.96	.172	.058	.023	.977	.981	.992
50	12	2.96	.480	.162	.179	.835	.881	1.017
50	12	2.96	.143	.048	.016	.984	1.000	1.005
50	12	2.96	.251	.085	.049	.951	.968	1.003
50	20	2.96	.153	.052	.049	.951	.974	.983
50	20	2.96	.448	.150	.422	.656	.803	1.151
50	20	2.96	.113	.038	.027	.973	.994	1.012
50	20	2.96	.205	.069	.089	.915	.948	1.007
LONG SEPARATION:								
100	25	1.48	.15	.101	.290	.748	.765	.93
100	20	1.48	.14	.095	.166	.848	.832	.95
100	15	1.48	.15	.101	.109	.896	.850	..95
100	10	1.48	.14	.095	.043	.957	.920	.956
100	5	1.48	.117	.079	.008	.993	.954	.957
100	30	1.48	.40	.270	2.88	.056	.189	.95
100	25	1.48	.405	.273	2.11	.121	.241	.98
100	20	1.48	.42	.280	1.48	.228	.422	1.49
100	20	1.48	.46	.310	1.78	.169	.375	2.13
100	20	1.48	.39	.263	1.28	.278	.329	1.23
100	15	1.48	.45	.304	.98	.375	.487	1.36
100	10	1.48	.416	.281	.377	.685	.701	1.02
100	5	1.48	.435	.294	.103	.902	.819	.898
100	30	1.48	.067	.045	.081	.923	.975	1.03
100	25	1.48	.062	.042	.050	.951	.968	.98
100	20	1.48	.039	.026	.013	.987	.976	.977
100	15	1.48	.042	.028	.009	.998	.987	.988
100	10	1.48	.033	.022	.003	1.000	.988	.98
100	5	1.48	.039	.026	~ 0	1.000	1.000	.991
100	30	1.48	.175	.118	.550	.577	.661	1.07
100	25	1.48	.168	.113	.364	.694	.713	.97
100	20	1.48	.14	.095	.165	.848	.782	.92
100	15	1.48	.16	.108	.124	.882	.824	.942
100	10	1.48	.143	.097	.045	.955	.917	.96
100	5	1.48	.147	.100	.012	.988	.947	.953

Freq.	θ	λ	σ	λ/σ	g	e^{-g}	$\frac{I_{total}}{I_{mirror}}$	$\frac{I_{coh}(obs)}{e^{-g}}$
SHORT SEPARATION (With Wind):								
100	12	1.48	.162	.109	.082	.921	.856	.923
100	12	1.48	.483	.326	.728	.483	.580	1.233
100	12	1.48	.143	.097	.064	.938	.939	1.022
100	12	1.48	.229	.155	.163	.850	.734	.853
100	30	1.48	.134	.091	.324	.723	.629	.755
100	30	1.48	.422	.215	3.21	.040	.174	.425
100	30	1.48	.104	.070	.195	.822	.819	.620
100	30	1.48	.214	.144	.826	.438	.516	.600
100	20	1.48	.159	.107	.213	.808	.722	.900
100	20	1.48	.441	.298	1.64	.194	.321	1.58
100	20	1.48	.106	.072	.095	.910	.885	.967
100	20	1.48	.233	.157	.457	.633	.662	.905
SHORT SEPARATION (Cross-wind)								
100	12	1.48	.166	.112	.086	.918	.911	.982
100	12	1.48	.498	.336	.774	.461	.631	1.27
100	12	1.48	.170	.115	.090	.914	.974	1.015
100	12	1.48	.249	.168	.193	.823	.897	1.029
100	20	1.48	.161	.109	.218	.804	.772	.965
100	20	1.48	.449	.304	1.705	.181	.361	1.564
100	20	1.48	.081	.055	.055	.946	.958	.981
100	20	1.48	.228	.154	.438	.645	.776	1.010
100	30	1.48	.140	.095	.354	.701	.622	.756
100	30	1.48	.429	.290	3.32	.036	.312	.764
100	30	1.48	.066	.045	.079	.924	.958	.870
100	30	1.48	.169	.114	.515	.597	.654	.708

BIBLIOGRAPHY

1. Medwin, H., "Specular Scattering of Underwater Sound from a Wind-Driven Surface", Journal of the Acoustical Society of America v. 41, pp. 1485-1495, June 1967.

2. Beckmann, P., and Spizzichino, A., The Scattering of Electromagnetic Waves from Rough Surfaces, Macmillan Co., New York, 1963.

3. Scheible, J.W., and Fowler, R.C., Specular Scatter of Underwater Sound from a Wind-Driven Model Sea Surface, Master's Thesis, Naval Postgraduate School, Monterey, June 1968.

4. Parkins, B.E., "Scattering from the Time-Varying Surface of the Ocean", Journal of the Acoustical Society of America, v. 42, no. 6, 1967.

5. Wagner, R.J., "Shadowing of Randomly Rough Surfaces", Journal of the Acoustical Society of America, v. 41, No. 1, 1967.

6. Phillips, O.M., The Dynamics of the Upper Ocean, Cambridge University Press, 1966.

7. Mayo, N.H., Spatial Wave Height Correlation Measurements on an Anisotropic, Wind-Driven Surface. Unpublished paper submitted in fulfillment of requirements of course 4353, Naval Postgraduate School, Monterey, November 1968.

INITIAL DISTRIBUTION LIST

		No. Copies
1.	Defense Documentation Center Cameron Station Alexandria, Virginia 22314	20
2.	Library, Code 0212 Naval Postgraduate School Monterey, California 93940	2
3.	Commander, Naval Ordnance Systems Command Department of the Navy Washington, D.C. 20360	1
4.	Professor H. Medwin Department of Physics Naval Postgraduate School Monterey, Ca. 93940	6
5.	Dr. Wayne Wright Physics Department Naval Postgraduate School Monterey, Ca. 93940	1
6.	LT James D. Hagy Ordnance Engineering Programs Office Naval Postgraduate School Monterey, Ca. 93940	1
7.	Mr. William Smith Department of Physics Naval Postgraduate School Monterey, Ca. 93940	1
8.	LCDR Ned H. Mayo USS HENDERSON (DD 785) FPO, San Francisco 96601	1
9.	Commander, Anti-Submarine Warfare Systems Projects Office Department of the Navy Washington, D.C. 20360	1
10.	Director, Acoustics Programs (Code 468) Office of Naval Research Washington, D.C. 20360	1
11.	Commander, Naval Ships Systems Command ATTN: PMS 88 Department of the Navy Washington, D.C. 20305	1

Security Classification

DOCUMENT CONTROL DATA - R & D

(Security classification of title, body of abstract and indexing annotation must be entered when the overall report is classified)

1. ORIGINATING ACTIVITY *(Corporate author)*

Naval Postgraduate School
Monterey, California 93940

2a. REPORT SECURITY CLASSIFICATION

Unclassified

2b. GROUP

3. REPORT TITLE

Near-Grazing, Specular Scattering of Underwater Sound from Sea and Swell

4. DESCRIPTIVE NOTES *(Type of report and inclusive dates)*

Master's Thesis; December 1969

5. AUTHOR(S) *(First name, middle initial, last name)*

Ned Henderson Mayo

6. REPORT DATE	7a. TOTAL NO. OF PAGES	7b. NO. OF REFS
December 1969	84	7

8a. CONTRACT OR GRANT NO.	9a. ORIGINATOR'S REPORT NUMBER(S)
b. PROJECT NO.	
c.	9b. OTHER REPORT NO(S) *(Any other numbers that may be assigned this report)*
d.	

10. DISTRIBUTION STATEMENT

This document has been approved for public release and sale; its distribution is unlimited.

11. SUPPLEMENTARY NOTES	12. SPONSORING MILITARY ACTIVITY
	Naval Postgraduate School Monterey, California 93940

13. ABSTRACT

The surface of a large, anechoic tank was excited to produce several different anisotropic sea and swell surfaces characterized by "typical" but distinctive frequency spectra and wave height probability densities. Surface roughness for specular scatter, g ($=4k^2\sigma^2\sin^2\theta$), was varied from zero to four by selection of underwater sound propagation constant, k, RMS wave height, σ, and grazing angle, θ. Concurrent measurement was made of 20 second averages of squared surface wave height, and coherent, specularly-scattered sound intensity. For $g \leq 1.$, coherent specular scatter from all surfaces, including pure swell (with a strongly non-Gaussian wave height probability density) was found to vary as e^{-g}, as previously predicted for Gaussian surfaces only. For certain combinations of θ, σ, and sound wavelength, λ, coherent components significantly larger than predicted were noted in both cross-wind and down-wind scattering for $g > 1.$; this is believed to be a previously-hypothesized interference phenomenon. Cross-sea scattering consistently produced a slightly stronger coherent component of intensity than scattering in the direction of the sea.

DD FORM 1 NOV 65 1473 (PAGE 1)

S/N 0101-807-6811

Security Classification

A-31408

14. KEY WORDS	LINK A		LINK B		LINK C	
	ROLE	WT	ROLE	WT	ROLE	WT
Underwater Sound						
Scattering						
Specular Scattering						
Rough Water Surface						
Wave Height Distribution						
Wave Spectrum						
Doppler Shift						
Scattered Sound Spectrum						
Scattered Sound Distribution						
Correlation						
Coherent						